

THE PROPERTIES OF Ly α NEBULAE: GAS KINEMATICS FROM NON-RESONANT LINES*

YUJIN YANG^{1,2}, ANN ZABLUDOFF³, KNUD JAHNKE², ROMEEL DAVÉ^{3,4,5,6}

Accepted for publication in ApJ.

ABSTRACT

With VLT/X-shooter, we obtain optical and near-infrared spectra of six Ly α blobs at $z \sim 2.3$. For a total sample of eight Ly α blobs (including two that we have previously studied), the majority (6/8) have broadened Ly α profiles with shapes ranging from a single peak to symmetric or asymmetric double-peaked. The remaining two systems, in which the Ly α profile is not significantly broader than the [O III] or H α emission lines, have the most spatially compact Ly α emission, the smallest offset between the Ly α and the [O III] or H α line velocities, and the only detected C IV and He II lines in the sample, implying that a hard ionizing source, possibly an AGN, is responsible for their lower optical depth. Using three measures — the velocity offset between the Ly α line and the non-resonant [O III] or H α line ($\Delta v_{\text{Ly}\alpha}$), the offset of stacked interstellar metal absorption lines, and a new indicator, the spectrally-resolved [O III] line profile — we study the kinematics of gas along the line of sight to galaxies within each blob center. These three indicators generally agree in velocity and direction, and are consistent with a simple picture in which the gas is stationary or slowly outflowing at a few hundred km s^{-1} from the embedded galaxies. The absence of stronger outflows is not a projection effect: the covering fraction for our sample is limited to $< 1/8$ (13%). The outflow velocities exclude models in which star formation or AGN produce “super” or “hyper” winds of up to $\sim 1000 \text{ km s}^{-1}$. The $\Delta v_{\text{Ly}\alpha}$ offsets here are smaller than typical of Lyman break galaxies (LBGs), but similar to those of compact Ly α emitters. The latter suggests a connection between blob galaxies and Ly α emitters and that outflow speed cannot be a dominant factor in driving extended Ly α emission. For one Ly α blob (CDFS-LAB14), whose Ly α profile and metal absorption line offsets suggest no significant bulk motion, we use a simple radiative transfer model to make the first column density measurement of gas in an embedded galaxy, finding it consistent with a damped Ly α absorption system. Overall, the absence of clear inflow signatures suggests that the channeling of gravitational cooling radiation into Ly α is not significant over the radii probed here. However, one peculiar system (CDFS-LAB10) has a blueshifted Ly α component that is not obviously associated with any galaxy, suggesting either displaced gas arising from tidal interactions among blob galaxies or gas flowing into the blob center. The former is expected in these overdense regions, where *HST* images resolve many galaxies. The latter might signify the predicted but elusive cold gas accretion along filaments.

Keywords: galaxies: formation — galaxies: high-redshift — intergalactic medium

1. INTRODUCTION

Giant Ly α nebulae, or “blobs,” are extended sources at $z \sim 2$ –6 with typical Ly α sizes of $\gtrsim 5''$ ($\gtrsim 50 \text{ kpc}$) and line luminosities of $L_{\text{Ly}\alpha} \gtrsim 10^{43} \text{ erg s}^{-1}$ (e.g., Keel et al. 1999; Steidel et al. 2000; Francis et al. 2001; Matsuda et al. 2004, 2011; Dey et al. 2005; Saito et al. 2006; Smith & Jarvis 2007; Hennawi et al. 2009; Ouchi et al. 2009; Prescott et al. 2009, 2012a; Yang et al. 2009, 2010; Erb et al. 2011). The low number counts, strong clustering, multiple embedded sources, and location in overdense environments of the largest Ly α blobs indicate that

they lie in massive ($M_{\text{halo}} \sim 10^{13} M_{\odot}$) dark matter halos, which will evolve into those typical of rich galaxy groups or clusters today (Yang et al. 2009, 2010; Prescott et al. 2008, 2012b). Therefore, Ly α blobs are unique tracers of the formation of the most massive galaxies and their early interaction with the surrounding intergalactic medium (IGM).

This interaction is probably tied on some scale to the source of the blobs’ extended Ly α emission, but that mechanism is poorly understood. Emission from Ly α blobs could arise from several phenomena, which may even operate together, including shock-heating by galactic superwinds (Taniguchi & Shioya 2000) or gas photoionized by active galactic nuclei (Haiman & Rees 2001; Geach et al. 2009). Another possibility is smooth gas accretion, which is likely to play an important role in the formation of galaxies (e.g., Kereš et al. 2005, 2009) and which should channel some of its gravitational cooling radiation into atomic emission lines such as Ly α (Haiman, Spaans, & Quataert 2000; Fardal et al. 2001; Dijkstra & Loeb 2009; Goerdt et al. 2010). Another scenario is the resonant scattering of Ly α photons produced by star formation or active galactic nuclei (AGN) (Steidel et al. 2010; Hayes et al. 2011) in the embedded galaxies.

¹ Argelander Institut für Astronomie, Universität Bonn, Auf dem Hügel 71, 53121 Bonn, Germany, yyang@astro.uni-bonn.de

² Max-Planck-Institut für Astronomie, Königstuhl 17, Heidelberg, Germany

³ Steward Observatory, University of Arizona, 933 North Cherry Avenue, Tucson AZ 85721

⁴ University of the Western Cape, Bellville, Cape Town 7535, South Africa

⁵ South African Astronomical Observatories, Observatory, Cape Town 7525, South Africa

⁶ African Institute for Mathematical Sciences, Muizenberg, Cape Town 7545, South Africa

* Based on observations made with an ESO telescope at the Paranal Observatory, under the program ID 086.A-0804.

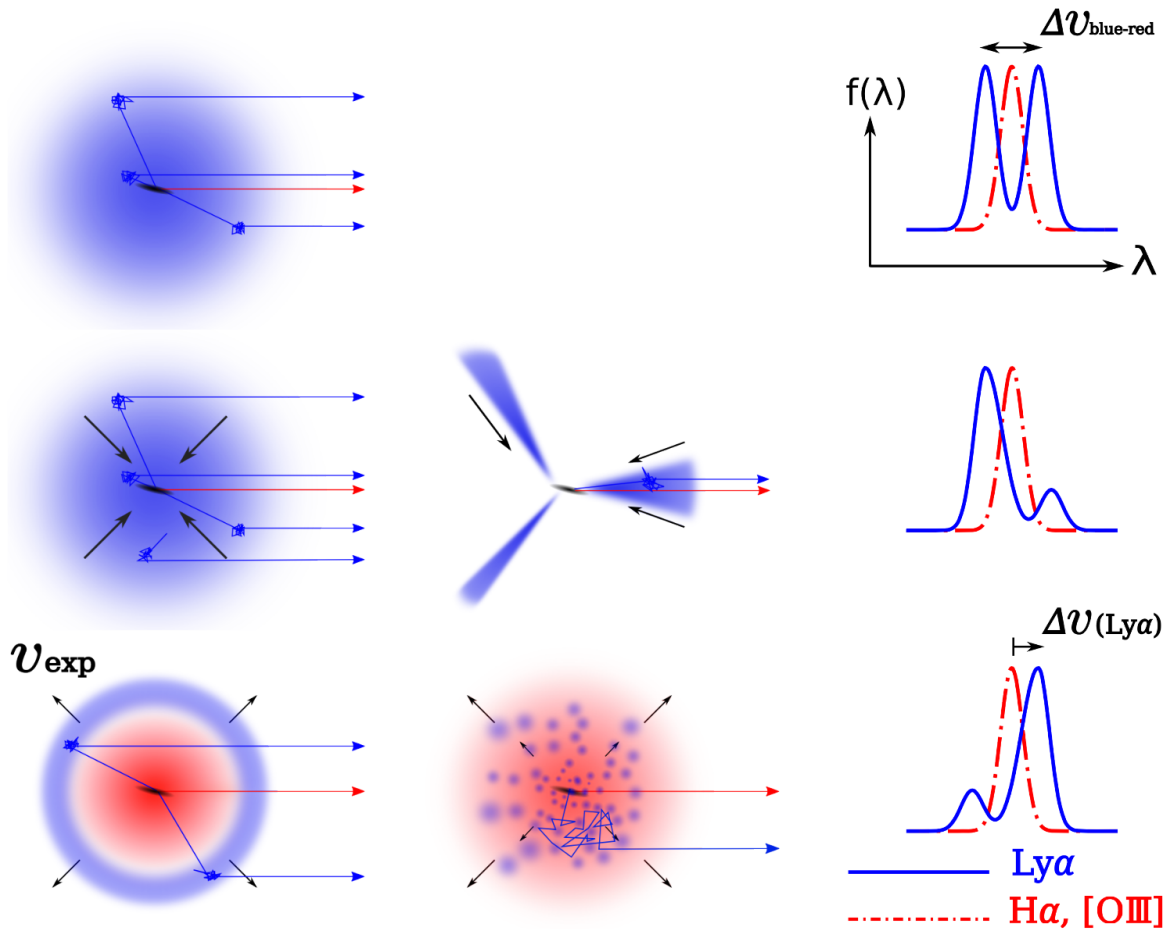


Figure 1. Schematic diagrams of the expected Ly α and non-resonant H α or [O III] profiles if the gas in the blobs is static, inflowing, or outflowing. The solid (blue) and dashed (red) lines represent the Ly α and non-resonant (optically-thin to H I) lines, respectively. **(Top: static cloud)** Because the surrounding gas cloud is optically thick to the Ly α line, Ly α photons in the Doppler wings should escape the cloud through random scatterings in the frequency domain. Therefore, if the surrounding gas is static, the Ly α line should have a double-peaked profile, while the non-resonant line photons will escape without any radiative transfer effects. **(Middle: spherical infall)** If the gas is infalling toward the embedded galaxy, Ly α photons within the cloud on the red side of the double-peaked profile will see higher optical depth due to the line-of-sight infalling gas, and the red peak will be depressed. **(Bottom: expanding shell)** In contrast, if the gas is outflowing, the blue side of the profile will be more diminished. In summary, if there is gas infall (or outflow), the Ly α profiles will be asymmetric and blue-shifted (or redshifted) against the non-resonant line due to radiative transfer in the optically thick medium, but the corresponding non-resonant line profiles should be symmetric. Note that one cannot determine whether the Ly α line is redshifted or blue-shifted against the background velocity field unless there is an optically thin reference line, i.e., H α or [O III]. *Both Ly α and non-resonant lines are therefore required to resolve the nature of the Ly α blobs.* **(Middle column)** However, the actual geometry of infall and outflow is unknown. For example, gas infall may take place in narrow streams (e.g., Dekel et al. 2009; Goerdt et al. 2010). Or, an outflow may be bipolar/highly collimated (e.g., M82, Bland & Tully 1988) or “clumpy” (Steidel et al. 2010). A large statistic sample of blob gas kinematics, like that presented in this paper, is required to constrain that geometry.

To resolve the debate about the nature of Ly α blobs requires — at the very least — that we discriminate between outflowing and inflowing models. Because Ly α is a resonant line and typically optically thick in the surrounding intergalactic medium, studies even of the same Ly α blob’s kinematics can disagree. On one hand, Wilman et al. (2005) argue that their integral field unit (IFU) spectra of a Ly α blob are consistent with a simple model where the Ly α emission is absorbed by a foreground slab of neutral gas swept out by a galactic scale outflow. On the other, Dijkstra et al. (2006b) explain the same data as arising from the infall of the surrounding intergalactic medium. Worse, Verhamme et al. (2006) claim that the same symmetric Ly α profiles are most consistent with static surrounding gas.

To distinguish among such possibilities requires a comparison of the center of the Ly α line profile with that of a non-resonant line like H α λ 6563 or [O III] λ 5007. These

rest-frame optical nebular lines are better measure of the Ly α blob’s systemic velocity, i.e., of the precise redshift, because it is not seriously altered by radiative transfer effects and is more concentrated about the galaxies in the Ly α blob’s core. We illustrate this line offset technique in Figure 1. While gas accretion models predict different line profile shapes depending on various assumptions, e.g., the location of ionizing sources, the detailed geometry, and the velocity field, they all predict that the overall Ly α line profile, originating from the central source or the surrounding gas, will be blue-shifted with respect to the center of a non-resonant line such as H α that is optically thin to the surrounding H I gas (Verhamme et al. 2006; Dijkstra et al. 2006a). This is because the red-side of the Ly α profile will see higher optical depth due to the infalling (approaching) gas. In other words, the H α kinematics represent the true underlying velocity field if the Ly α blob is accreting gas from the intergalactic medium.

The same is true if the gas is outflowing, except that the $\text{Ly}\alpha$ line will be redshifted with respect to $\text{H}\alpha$. Thus, if we measure the direction of the $\text{Ly}\alpha$ – $\text{H}\alpha$ and/or $\text{Ly}\alpha$ – $[\text{O III}]$ line offset (hereafter defined as $\Delta v_{\text{Ly}\alpha}$), we can distinguish an inflow from an outflow.

The first such analysis for two $\text{Ly}\alpha$ blobs shows that $\text{Ly}\alpha$ is coincident with or redshifted by $\sim 200 \text{ km s}^{-1}$ from the $\text{H}\alpha$ line center (Yang et al. 2011, see also McLinden et al. 2013). These offsets are much smaller than the $\sim 1000 \text{ km s}^{-1}$ expected from superwind models (Taniguchi & Shioya 2000) and even smaller than those typical of Lyman break galaxies (LBGs), which are widely believed to have galactic outflows (Steidel et al. 2004, 2010). Thus, if $\Delta v_{\text{Ly}\alpha}$ is a proxy for outflow velocities (v_{exp}), our initial results suggest that star formation- or AGN-produced winds may not be required for powering $\text{Ly}\alpha$ blobs, making other interpretations of their emission more likely.

However, we do not yet know if these results are representative of *all* $\text{Ly}\alpha$ blobs or if we have failed to detect strong flows due to the projected orientations of these two sources. For example, the gas flow may not be isotropic. As in bipolar outflows in M82 (e.g., Bland & Tully 1988), a galactic-scale outflow may occur in the direction of minimum pressure in the surrounding interstellar medium (ISM), often perpendicular to the stellar disks. Or, if gas accretion is taking place in $\text{Ly}\alpha$ blobs, numerical simulations suggest that the gas infall may occur preferentially along filamentary streams (Kereš et al. 2005, 2009; Dekel et al. 2009). Thus, if the bulk motion of gas (either infalling or outflowing) happens to be misaligned with our line of sight (LOS), then we may underestimate or even fail to detect the relative velocity shifts. Therefore, it is critical to measure $\Delta v_{\text{Ly}\alpha}$ for a larger sample to average over any geometric effects and obtain better constraints on the incidence, direction, speed, and isotropy of bulk gas motions in blobs.

In this paper, in order to overcome this geometry effects, we present new X-shooter optical and near-infrared (NIR) spectroscopy of the six more $\text{Ly}\alpha$ blobs at $z \approx 2.3$. Note that the survey redshift of this $\text{Ly}\alpha$ sample has been carefully selected to allow all important rest-frame optical diagnostic lines (e.g., $[\text{O II}] \lambda 3727$, $[\text{O III}] \lambda 5007$, $\text{H}\beta \lambda 4868$, $\text{H}\alpha \lambda 6563$) to fall in NIR windows and to avoid bright OH sky lines and atmospheric absorption (Yang et al. 2009, 2010). With the resulting large sample of $\Delta v_{\text{Ly}\alpha}$ measurements (a total of eight), we determine the relative frequency of gas infall versus outflow.

Benefiting from X-shooter’s high spectral resolution and wide spectral coverage ($3000\text{\AA} - 2.5\mu\text{m}$), we constrain the gas kinematics in $\text{Ly}\alpha$ blobs using three different tracers: (1) the offset of the $\text{Ly}\alpha$ profile with respect to a non-resonant nebular line, (2) the offset of an interstellar metal absorption line in the rest-frame UV with respect to the nebular emission line, and (3) a new indicator, the profile of the spectrally-resolved $[\text{O III}]$ emission line.

This paper is organized as follows. In Section 2, we review our sample selection and describe the X-shooter observations and data reduction. In Section 3, we present the results from the X-shooter spectroscopy, confirming the $\text{Ly}\alpha$ blobs’ redshift (Section 3.2). We present 1-D and 2-D spectra in Section 3.2 and Section 3.3, respec-

tively. We briefly summarize the properties of individual systems in Section 3.4. In Section 3.5, we constrain the gas kinematics using the three different techniques noted above. In Section 3.5.1, we compare the $\text{Ly}\alpha$ profiles with the $\text{H}\alpha$ or $[\text{O III}]$ line centers to discriminate between simple infall and outflow scenarios and present the $\Delta v_{\text{Ly}\alpha}$ statistics for the sample. In Section 3.5.2, we describe the interstellar absorption lines detected in three galaxies. In Section 3.5.3, we inspect the $[\text{O III}]$ emission line profiles in detail to look for possible signatures of warm outflows. In Section 3.6, we constrain the H I column density of a $\text{Ly}\alpha$ blob by comparing its $\text{Ly}\alpha$ profile with a simple radiative transfer (RT) model. In Section 3.7, we focus on a $\text{Ly}\alpha$ blob with a blue-shifted $\text{Ly}\alpha$ component not directly associated with any detected galaxy, a possible marker of gas inflow. Section 5 summarizes our conclusions. Throughout this paper, we adopt the cosmological parameters: $H_0 = 70 \text{ km s}^{-1} \text{ Mpc}^{-1}$, $\Omega_M = 0.3$, and $\Omega_\Lambda = 0.7$.

2. OBSERVATIONS AND DATA REDUCTION

2.1. Sample

We observe six $\text{Ly}\alpha$ blobs from the Yang et al. (2010) sample. These targets were chosen such that they are not X-ray detected [$L(2 - 32\text{keV}) < (0.3 - 4.2) \times 10^{43} \text{ erg s}^{-1}$; Lehmer et al. (2005); Luo et al. (2008)], and thus are not obvious AGN, as our primary goal is to cleanly detect gas infall or outflow. These six blobs lie in the Extended Chandra Deep Field South (ECDFS) and were discovered via deep narrowband imaging with the CTIO-4m MOSAIC-II camera and a custom narrowband filter (NB403). This filter has a central wavelength of $\lambda_c \approx 4030\text{\AA}$, designed for selecting $\text{Ly}\alpha$ -emitting sources at $z \approx 2.3$. In Figure 2, we show the images of these six $\text{Ly}\alpha$ blobs (CDFS-LAB06, 07, 10, 11, 12, 13, 14) at various wavelengths (*UBK*, $\text{Ly}\alpha$, *Spitzer* IRAC $3.6\mu\text{m}$ and *HST* F606W; Gawiser et al. 2006, Yang et al. 2010, Damen et al. 2011, Rix et al. 2004).

With X-shooter, we are targeting intermediate luminosity ($L_{\text{Ly}\alpha} \sim 10^{43} \text{ erg s}^{-1}$) $\text{Ly}\alpha$ blobs: the higher $\text{Ly}\alpha$ blob ID indicates the lower $\text{Ly}\alpha$ luminosity in our sample. Our sample was obtained from a blind survey, so combined with the two brightest $\text{Ly}\alpha$ blobs presented in Yang et al. (2011), the full sample (a total of eight) spans a wide and more representative range of $\text{Ly}\alpha$ luminosity and size. Furthermore, the transition from compact $\text{Ly}\alpha$ emitters (LAEs; isophotal area of a few arcsec^2) to extended $\text{Ly}\alpha$ blobs ($> 10 \text{ arcsec}^2$) is continuous (Matsuda et al. 2004; Yang et al. 2010), thus the gas kinematics for our faintest $\text{Ly}\alpha$ blobs might share the properties with those of bright LAEs. We refer readers to Yang et al. (2010) for details of the sample selection and to Yang et al. (2011) for the first results of our spectroscopic campaign.

2.2. UV-to-NIR Spectroscopy

We obtained high resolution optical–NIR ($3000\text{\AA} - 2.5\mu\text{m}$) spectra of the six $\text{Ly}\alpha$ blobs using X-shooter, a single object echelle spectrograph (Vernet et al. 2011), on the VLT UT2 telescope in service mode between 2010 November 6 and 2011 January 28. In Table 1, we summarize the X-shooter observations. In Figure 2, we show the location of the spectrograph slit on the sky, which

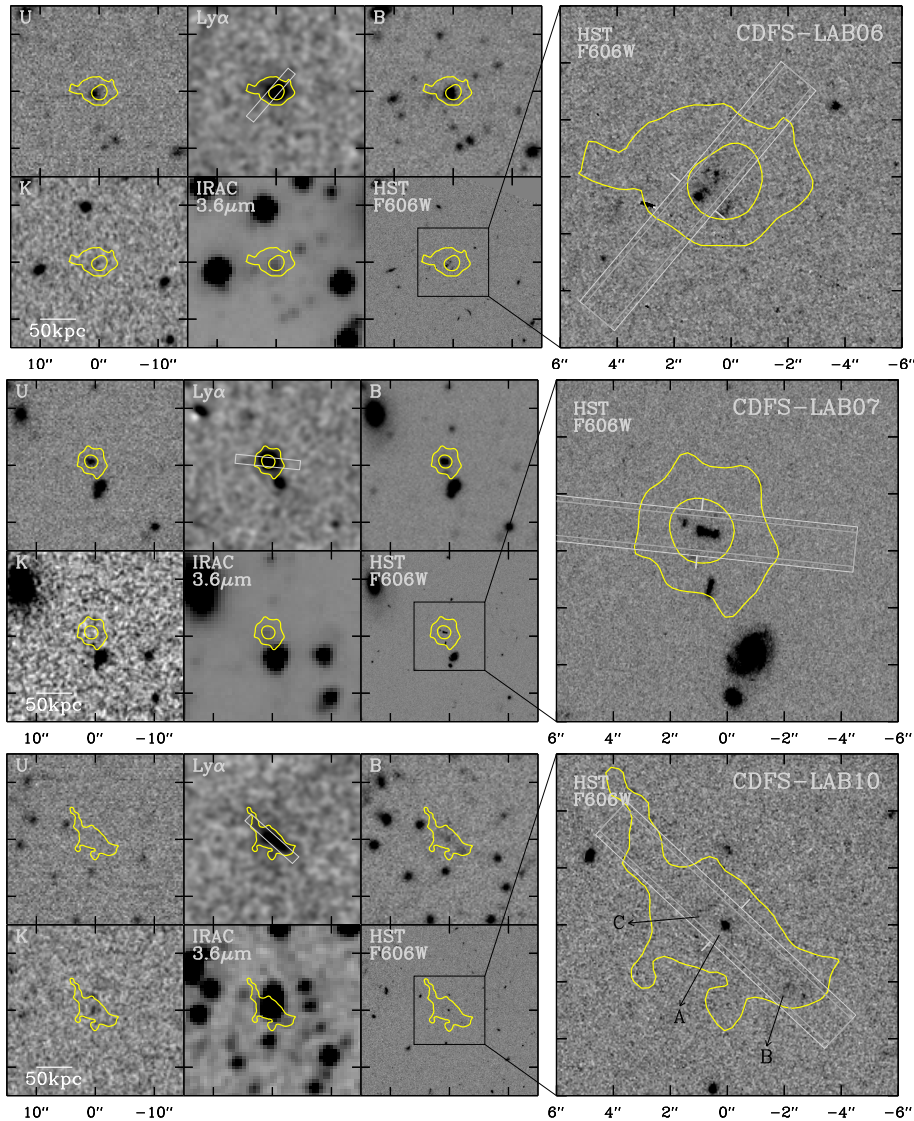


Figure 2. Images of Ly α blobs at various wavelengths: *U*, continuum-subtracted Ly α line, *B*, *K*, *Spitzer* IRAC 3.6 μ m, and *HST* F606W images. Contours represent a surface brightness of 4 and 20×10^{-18} erg s $^{-1}$ cm $^{-2}$ arcsec $^{-2}$ from CTIO-4m narrowband imaging. Ticks indicate 10'' (82 physical kpc) intervals. Two gray boxes indicate the X-shooter slit positions of the UVB (1''6) and NIR (1''2) arms (12''-longslit), respectively. Center of a slit is marked with small outward ticks. X-shooter provides the unique capability of targeting the optical and NIR diagnostic lines simultaneously.

was placed on UV-brightest galaxy or galaxies embedded at or near the Ly α center. These galaxies or galaxy fragments also lie in the region of brightest Ly α emission. Later, we assume that their redshifts mark the systemic redshift of the Ly α blob.

X-shooter consists of three arms (UVB, VIS, NIR), which covers the spectral ranges of 3000Å–5500Å, 5500Å–1 μ m, and 1 μ m–2.5 μ m, respectively. This enormous spectral coverage allows us to obtain both Ly α and H α lines with a *single* exposure in contrast to our previous approach (Yang et al. 2011) involving both optical and NIR spectrograph. Furthermore, X-shooter can detect at least one of the nebular lines ([O II], H β , [O III], H α), which will provide the systemic velocity of the embedded galaxies. Because at the redshift of our targets ($z \simeq 2.3$) most of the emission lines of interest (Ly α , C IV, He II, [O II], [O III], H α) are located in the UVB or NIR arms, we focus only on the UVB ($\lambda_{\text{rest}} = 900\text{Å}$ –

1660Å) and NIR ($\lambda_{\text{rest}} = 3020\text{Å}$ –7500Å) part of spectra in this paper.

The observations were carried out over eight nights and 14 observing blocks (OBs) of one hour duration each. The sky condition was either clear or photometric, and the guide camera seeing ranged from 0''6 to 1''2 with a median of 0''8 depending on the OB. We adopted 1''6 and 1''2-wide slits for UVB and NIR, yielding a spectral resolution of $R \sim 3300$ and $R \sim 3900$, respectively. The slit length is rather small (12'') compared to typical longslits. In each OB, we placed the slit on a target using a blind offset from a nearby star. Using acquisition images taken after the blind-offset, we estimate that the telescope pointing and position angle of the slit are accurate within 0.2'' and 0.5° on average, respectively. The individual exposure times were 680s and 240s for UVB and NIR, respectively, and the telescope was nodded along the slit by $\pm 2''$ while keeping the science targets always on the slit but at different detector positions. Total expo-

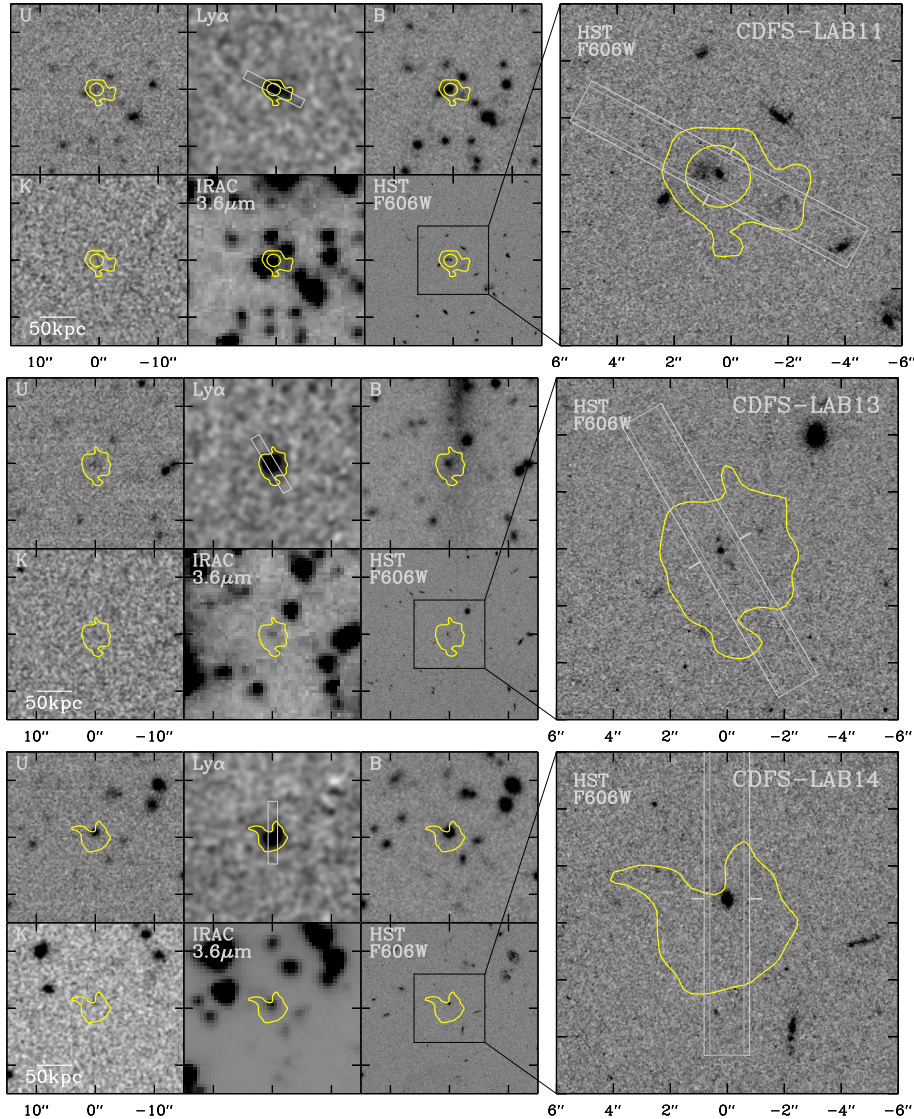


Figure 2. Continued.

sure times were 0.8 – 3.2 hours depending on the targets. In general, we were always able to detect both $\text{Ly}\alpha$ and at least one of the optical nebular lines within one OB.

For accurate wavelength calibration, we took ThAr lamp frames through pinhole mask right before the science exposures and at the same telescope pointing to compensate for the effect of instrument flexure. For the UVB arm, we obtained another ThAr arc frame at the end of each OB in order to verify the wavelength solution where no bright sky lines are available. Telluric standard stars (B-type) were taken after or before the science targets with similar airmass to correct for atmospheric absorption in the NIR. Spectrophotometric standard stars were observed with 5''-wide slits once during the night as a part of the observatory’s baseline calibration plan.

2.3. Data Reduction

We reduce the data using the ESO X-shooter pipeline (version 1.3.7). In the UVB arm, the frames are overscan-corrected, bias-subtracted, and flat-fielded with halogen and deuterium lamps. The sky background is then subtracted in the “stare”-mode of the pipeline by

modeling the sky in 2-D as described in Kelson (2003). In the NIR arm, dark current and sky background are removed from each science frame by subtracting the dithered “sky” frame (“nodding”-mode of the pipeline). Then, we flat-field the data and correct for cosmic-ray hits and bad pixels. In both arms, these flat-fielded, sky-subtracted frames were corrected for the spatial distortions using multi-pinhole arc frames.

Because we will compare the velocity centers of the $\text{Ly}\alpha$ and $\text{H}\alpha$ lines, we carefully verify the wavelength calibration. In the NIR, we compare the wavelength solutions obtained from the OH sky lines in the science frames to those from the daytime arc lamps and flexure-compensation frames, i.e., the pipeline solutions. In the UVB, we also compare the wavelength solutions obtained from the attached ThAr arc frames with the pipeline solutions. Our wavelength calibration is accurate within $\sim 4 \text{ km s}^{-1}$ in both arms. Furthermore, in the cases where we visited sources multiple times, all spectra agree each other. These frames are then rectified (resampled) and combined to create 2-D spectra. We collapse the 2-D spectra in the wavelength direction to measure the spa-

tial extent of each emission line. Then we extract 1-D spectra from $[-2\sigma, +2\sigma]$ apertures, where the σ is the Gaussian width of the spatial profile. The aperture sizes are $2''-3''5$ in the UVB and $1''5-2''5$ in the NIR depending on the target. Finally, the 1-D spectra are corrected to heliocentric velocities and transformed to the vacuum wavelength.

3. RESULTS

3.1. Systemic Redshift from [O III] and H α

Various emission lines in the UVB and NIR arms confirm that Ly α blobs lie at the survey redshift, $z \sim 2.3$. In addition to Ly α and H α , we cover other UV emission lines and the non-resonant [O II] $\lambda\lambda 3727, 3729$, [O III] $\lambda\lambda 4959, 5007$, and H β $\lambda 4861$ lines. In Figure 3, we show 1-D and 2-D spectra of the six Ly α blobs. The first three columns show the rest-frame UV emission lines (Ly α , C IV, He II) from the X-shooter UVB arm, and the remaining columns show the rest-frame optical nebular emission lines ([O II], H β , [O III], H α) from the NIR arm.

Among the rest-frame optical nebular lines, the [O III] line is the brightest and detected with highest signal-to-noise (S/N) ratio in all cases, partly due to the low sky background and thermal instrument background in H -band. We determine the systemic redshift using [O III] doublets. In one case (CDFS-LAB14), the brighter [O III] line ($\lambda 5007$) falls on top of an OH sky line, thus making it impossible to determine the line center. In this case we used the fainter [O III] line ($\lambda 4959$). The vertical dashed lines in Figure 3 indicate the line centers determined by [O III] lines, which are then overlayed on other emission line profiles. As expected, we find that the line centers of all non-resonant emission lines agree well each other, to within $\sim 10 \text{ km s}^{-1}$, showing that all of these lines are good indicators of systemic velocity. Thus, the brightest [O III] line can serve as best emission line to target for this survey redshift and instrument.

3.2. 1-D Ly α Profiles

The Ly α profiles are significantly broad compared to the non-resonant lines (H α and/or [O III]) in six cases out of the sample of eight Ly α blobs, including the two from our previous work (Yang et al. 2011). These integrated 1-D profile shapes range from an asymmetric single-peaked profile (CDFS-LAB06, 07, 10), to a double-peaked profile with a stronger red peak (CDFS-LAB02, 13), to a double-peaked profile with two similar intensity peaks (CDFS-LAB14). The Ly α profiles of even this small sample show extremely diverse morphologies consistent with simple radiative model predictions (Verhamme et al. 2006, 2008; Dijkstra et al. 2006a) with varying geometry and outflow velocities (see also Matsuda et al. 2006; Saito et al. 2008; Weijmans et al. 2010).

The remaining two Ly α profiles are narrower *relative to* the [O III] lines and show slightly extended wings (CDFS-LAB01 and 11). Note that the Ly α line width of CDFS-LAB01 is one of the largest among our sample, but the blue side of its Ly α profile agrees well with its H α profile (Yang et al. 2011). While there is an underlying broad component in CDFS-LAB11, the width of the dominant narrow component is small, comparable to that of the [O III] line (see §4.4). These are the two Ly α blobs where

He II and C IV emission lines are also detected indicating that they contain a hard ionizing source, possibly an AGN. If photo-ionization by an AGN is indeed responsible for the He II and C IV emission, and possibly the extended Ly α emission as well, the discovery of narrow Ly α profiles suggests that the Ly α blob gas is highly-ionized, i.e., that the resonant scattering of Ly α is not effective enough to alter the profile significantly. We will further investigate the details of these He II, C IV emission lines and the implications for AGN in a future paper (Y. Yang in preparation).

The fraction of double-peaked profiles is significant: $\sim 38\%$ (3/8), which is roughly consistent with the findings for LBGs and LAEs at $z = 2-3$. Among LBGs, Kulas et al. (2012) find that $\sim 30\%$ of LBGs with Ly α emission show multiple-peaked profiles. Yamada et al. (2012) also find that $\sim 50\%$ of LAE's profiles have multiple peaks.

3.3. 2-D Ly α and [O III] Profiles

Using 2-D spectra, we detect the extended Ly α lines and identify the exact locations from which the Ly α or [O III] line originates. In Figure 4, we show close-ups of the 2-D [O III] and Ly α profiles in the first and second columns, respectively. To aid the comparison between the [O III] and Ly α profiles, we overlay the rough boundary of the [O III] spectrum on each Ly α panel with ellipses. The third column shows the spatial profiles along the slit, i.e., collapsed in the wavelength direction. The last column shows the 1-D Ly α and [O III] profiles that are extracted from the different parts of the slit, as indicated with vertical arrows in the third column.

In four cases (CDFS-LAB06, 10, 13, 14), the Ly α spectrum is spatially extended relative to the [O III] line, confirming the narrowband imaging result that the Ly α -emitting gas extends beyond the embedded galaxies that are probably responsible for the [O III] emission. Note that the X-shooter spectroscopy reaches much shallower Ly α surface brightness limit ($\sim 1.5-3 \times 10^{-17} \text{ erg s}^{-1} \text{ cm}^{-2} \text{ arcsec}^{-2}$) than the narrowband imaging ($\sim 5 \times 10^{-18} \text{ erg s}^{-1} \text{ cm}^{-2} \text{ arcsec}^{-2}$; 3σ limit).

In two Ly α blobs (CDFS-LAB06 and 10), the [O III] lines are spatially resolved. However, there is no evidence that the [O III] or H α lines are extended beyond the UV continuum emission arising from stars in the embedded galaxies seen in Figure 2. Deeper NIR spectroscopic, preferentially IFU, observations are required to better define the spatial extent of these lines and to measure the spatially-resolved gas kinematics. Throughout the paper, we assume that the [O III] and H α lines originate from the central embedded galaxies, not from the extended Ly α -emitting gas, and thus that their line centers represent the systemic velocity of the Ly α blob. In the next section, we briefly describe individual systems in detail.

3.4. Notes for Individual Objects

3.4.1. CDFS-LAB06

CDFS-LAB06 has two rest-frame UV sources with small separation ($0''.8$; 6.5 kpc) in the *HST* image (Fig. 2). Both components (or clumps) were placed in the X-shooter slit and are detected in [O III] and Ly α (Fig. 4). These two sources are separated by only $\sim 50 \text{ km s}^{-1}$ in velocity space, thus it is not clear whether they belong to

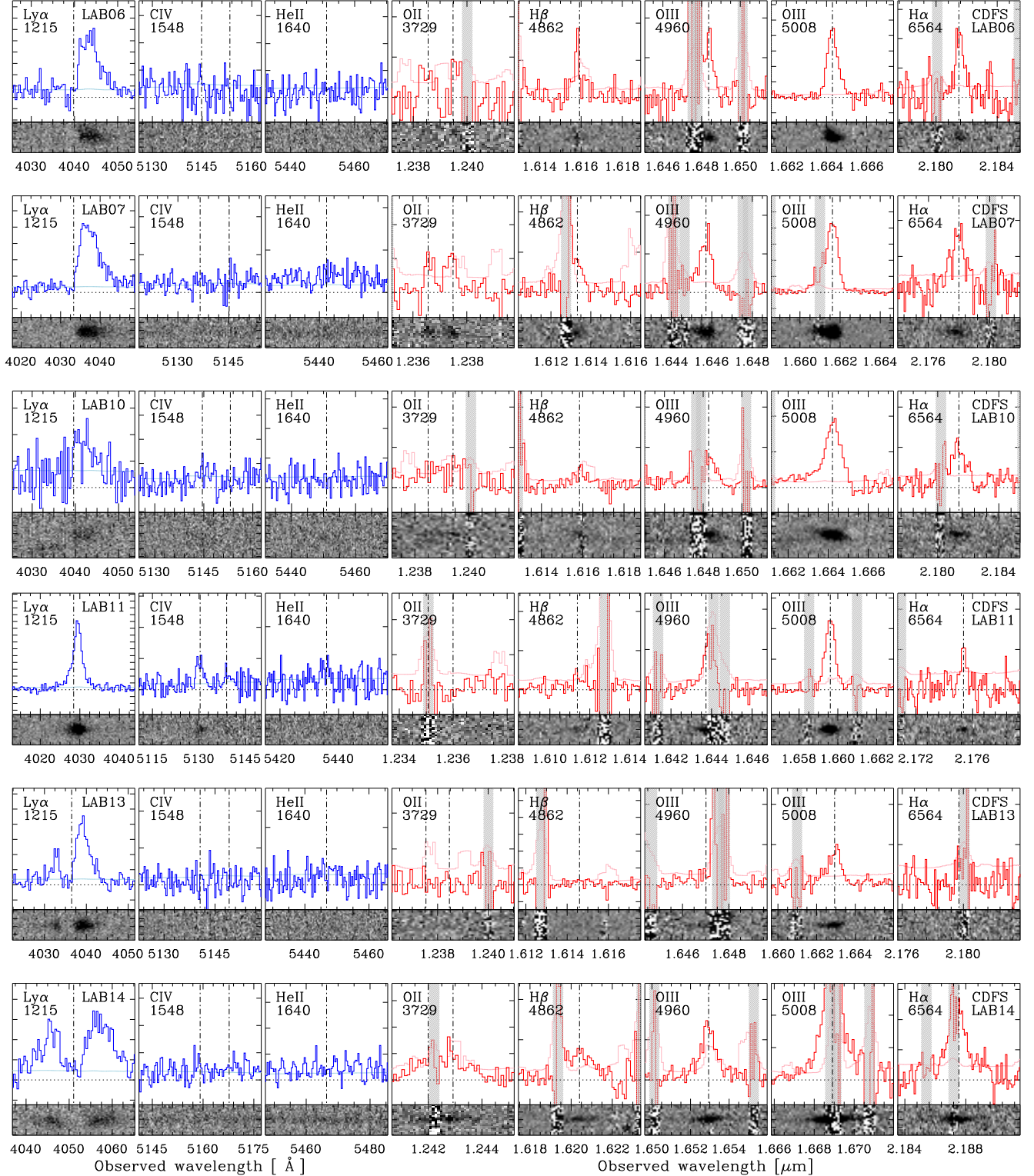


Figure 3. 1-D integrated line profiles for the rest-frame UV ($\text{Ly}\alpha$, C IV, He II) and optical ([O II], H β , [O III], H α) lines detected in the sightline toward the central, embedded galaxies. The velocity ranges are ± 1000 km s $^{-1}$ and ± 550 km s $^{-1}$ for the UV and optical spectra, respectively. The y-axis ticks are spaced every 1×10^{-17} and 0.5×10^{-17} ergs $^{-1}$ cm $^{-2}$ Å $^{-1}$ for the rest-frame UV and optical spectra, respectively. At the bottom of each spectrum, we show the 2-D spectra with 4'' or 6'' width. The vertical lines indicate the systemic velocity determined from the [O III] line. The other [O II], H α and H β lines are consistent with the [O III] center, suggesting that all provide a good reference to the center of the Ly α blob defined by the galaxy or galaxies embedded in the blob core. In all cases, the Ly α lines are broader than the H α or [O III] lines, implying that the Ly α is resonantly scattered by an optically thick medium. In CDFS-LAB11, the most compact of the sources, which is also detected in C IV and He II, the Ly α line is sharply peaked with broad wings.

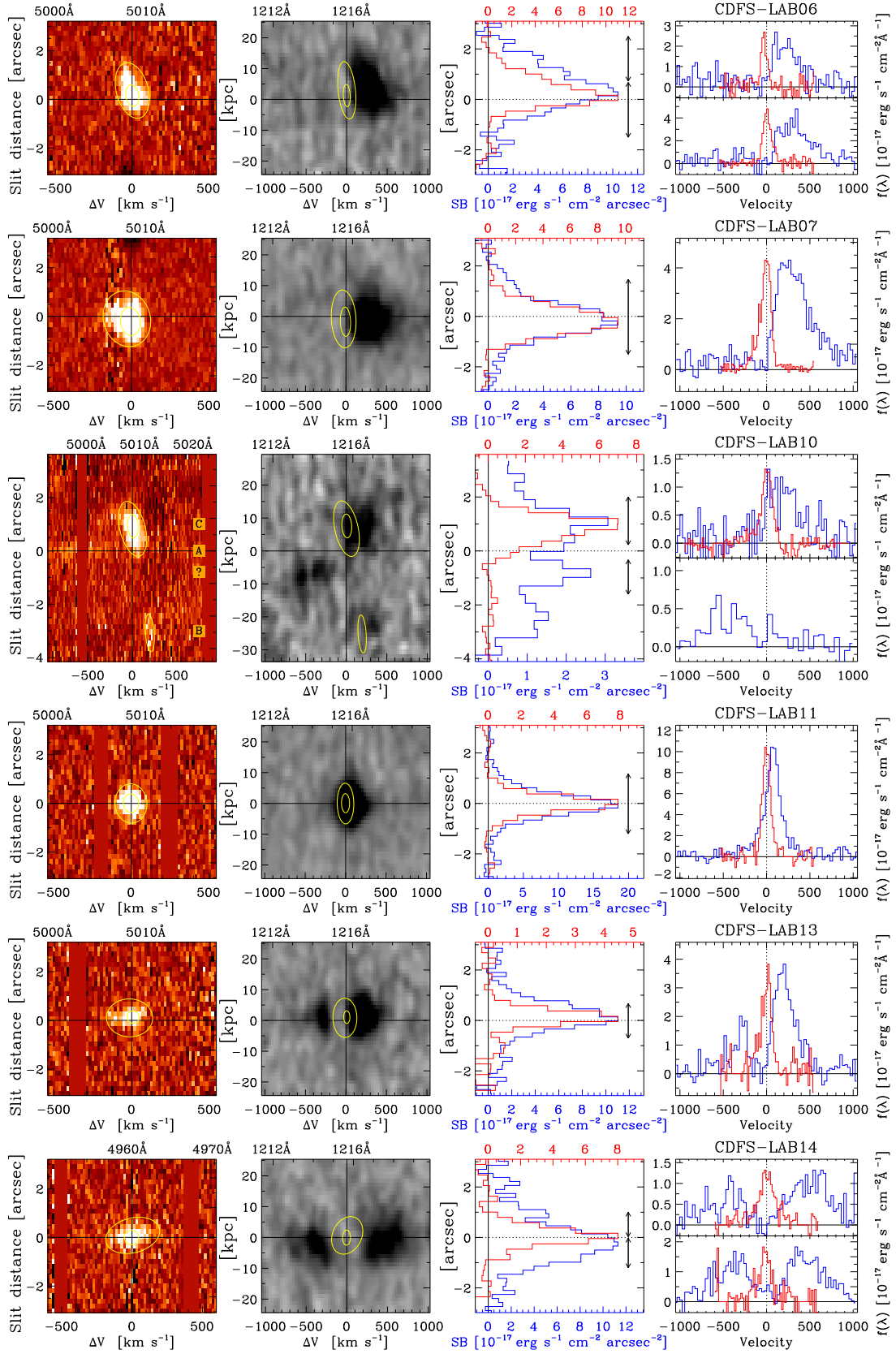


Figure 4. 2-D [O III] (first column) and Ly α (second column) spectra for Ly α blobs at $z \sim 2.31$. The Ly α spectra were smoothed to enhance low surface brightness features. Contours bounding the [O III] spectra are overlaid on the Ly α spectra to aid comparison between the two lines. The third column shows the spatial profile along the slits (collapsed in the spectral direction). The slit profiles are normalized for easy comparison, so the plots show different surface brightness scales on the top and bottom axes as indicated by different colors. The last column shows the extracted 1-D spectra from different regions defined by the arrows in third column. The Ly α profiles are significantly broader than the [O III] lines due to resonant scattering. Spectra toward three Ly α blobs show spatially extended Ly α spectra (CDFS-LAB06, 10, 14). In CDFS-LAB06, both [O III] and Ly α are extended due to a neighboring galaxy to the north. In the other two Ly α blobs, Ly α is more extended than the compact [O III] line, implying that Ly α is originating from the gas outside the galaxies.

one galaxy or are interacting with each other. We adopt the redshift of the brighter UV source as the systemic velocity of CDFS-LAB06. The $\text{Ly}\alpha$ emission detected in the spectrum (between $\Delta\theta = -1$ and $+2''$) is spatially extended due to the other galaxy, so it does not represent the IGM or circum-galactic medium (CGM).

3.4.2. CDFS-LAB07

The galaxy within CDFS-LAB07 has a bar-like morphology in the *HST* image with which we align the slit. This galaxy or galaxy fragments were marginally resolved in the $[\text{O III}]$ emission line. All optical nebular emission lines ($[\text{O II}]$, $\text{H}\beta$, $[\text{O III}]$, and $\text{H}\alpha$) are detected. Faint UV continuum emission is marginally detected, allowing us to study the gas kinematics with metal absorption lines (§3.5.2). The $[\text{O III}]$ and $\text{H}\alpha$ lines show asymmetric profiles extending toward the blue. This profile can be fitted with a narrow Gaussian component at the velocity center superposed on the blueshifted broad component (§3.5.3).

3.4.3. CDFS-LAB10

CDFS-LAB10 is the most puzzling and complex source in the X-shooter sample. The $\text{Ly}\alpha$ emission in the narrow-band image is elongated over $10''$ (~ 80 kpc). In the NIR spectrum, three sources are detected: two with $[\text{O III}]$ emission lines (galaxies B and C), and the other (galaxy A) with very faint continuum (Fig. 4). This NIR continuum source (galaxy A) is located at the slit center, while the strongest $[\text{O III}]$ -emitting source (galaxy C) is offset by $\sim 1''$ toward north-east from the center and barely detected in the *HST* image. The 2-D $[\text{O III}]$ spectrum of galaxy C shows a velocity shear indicative of rotating disk. In the 2-D $\text{Ly}\alpha$ spectrum, there are also three distinct components. Although the 1-D $\text{Ly}\alpha$ spectrum of the entire blob looks single-peaked with a broad linewidth, it is in fact composed of these three components. We will investigate these various emission line and continuum sources in §3.7.

3.4.4. CDFS-LAB11

There are one compact UV source at the slit center and a diffuse emission toward northeast in the *HST* image. It appears that the $[\text{O III}]$ emission originates from the central compact source. Unlike commonly observed broad $\text{Ly}\alpha$ profiles found in $\text{Ly}\alpha$ blobs and emitters, CDFS-LAB11 has a peculiar $\text{Ly}\alpha$ profile that is almost symmetric and narrow. As will be discussed in §4.4, both narrow and underlying broad components are required to explain the $\text{Ly}\alpha$ profile. The $\text{Ly}\alpha$ is redshifted against $\text{H}\alpha$ by small amount: $\Delta v_{\text{Ly}\alpha} = 84 \pm 6 \text{ km s}^{-1}$. Both $[\text{O III}]$ and $\text{Ly}\alpha$ are spatially compact (Fig. 4). Both C IV $\lambda 1546$ and He II $\lambda 1640$ emission lines are also detected (Fig. 3), implying the presence of hard ionizing source. A total of two $\text{Ly}\alpha$ blobs from our ECDFS sample (CDFS-LAB01 and 11; 2/8) show these emission lines. Note that C IV and narrow He II line emission are commonly detected in bright $\text{Ly}\alpha$ blobs (Dey et al. 2005; Scarlata et al. 2009; Prescott et al. 2009; Yang et al. 2011), while the nature of the hard-ionizing source is unknown.

3.4.5. CDFS-LAB13

CDFS-LAB13 has a double-peaked profile with a stronger red peak, and asymmetric $[\text{O III}]$ profile (§3.5.3).

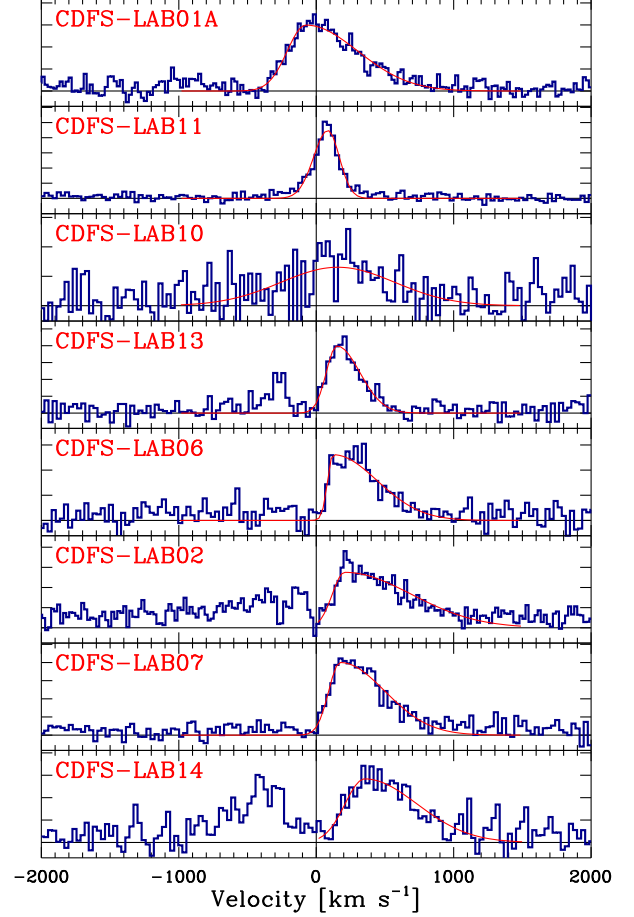


Figure 5. Comparison of $\text{Ly}\alpha$ line profiles (blue histogram), centered on the $\text{H}\alpha$ or $[\text{O III}]$ line arising from the embedded galaxy. The $\text{Ly}\alpha$ profiles are broad and diverse, ranging from symmetrically double-peaked (CDFS-LAB14), to double-peaked, but dominated by the red peak (CDFS-LAB02 and 13), to a single red peak (CDFS-LAB06, 07, 10), to almost symmetric profiles (CDFS-LAB01 and 11). The profiles are consistent with a single family of objects explained by a simple RT model in which the gas along the line-of-sight to the blob center is static (double-peaked with similar intensity), outflowing in a spherical shell from the center (red peak dominated), or outflowing and relatively optically thin (symmetric). The thin red lines indicate the fits with asymmetric Gaussian profiles used to determine the velocity offset between $\text{Ly}\alpha$ and either $\text{H}\alpha$ or $[\text{O III}]$, $\Delta v_{\text{Ly}\alpha}$ (see §3.5.1).

$\text{Ly}\alpha$ in CDFS-LAB13 is likely more extended, but the low S/N of the $[\text{O III}]$ line makes the comparison difficult. There are multiple galaxy fragments in the *HST* UV continuum image, but they were not spatially resolved in the X-shooter observations.

3.4.6. CDFS-LAB14

In the *HST* and narrowband images, a UV source is located at the upper boundary of the $\text{Ly}\alpha$ emission contours. In the X-shooter 2-D spectra (Figure 4), the $[\text{O III}]$ line is centered on this UV continuum source and $\text{Ly}\alpha$ is more extended toward the south in agreement with narrowband imaging. CDFS-LAB14 is one of two cases where extended $\text{Ly}\alpha$ emission is well detected in the spectroscopy. The $\text{Ly}\alpha$ profile has two peaks with similar intensities. The peak separation narrows as the slit distance from the central galaxy increases. Faint UV continuum is also detected at the location of the UV

source allowing us to measure outflow speed from metal absorption lines (§3.5.2). Combining the Ly α and the absorption profiles, we will put constraints on the gas kinematics and the neutral column density of this system (§3.6). [O III] has a broad wing on top of the narrow component (§3.5.3)

3.5. Gas Kinematics

In this section, we constrain the gas kinematics in the Ly α blobs using three different techniques and compare those results. First, for the six blobs in the X-shooter survey, we compare the optically thick Ly α and non-resonant [O III] line (either $\lambda 5007$ or $\lambda 4959$ in the case of CDFS-LAB14) to measure Ly α velocity offsets from the systemic velocity of the Ly α blobs. For the two Ly α blobs from our previous work (CDFS-LAB01A and 02; Yang et al. (2011)), where an [O III] line is unavailable, we use H α . As mentioned previously, the line centers of both [O III] lines and H α are all consistent. Second, we constrain the outflow speed from the interstellar metal absorption lines in three galaxies where we are able to detect the rest-frame UV continuum in the spectrum. Lastly, we present a new tracer of kinematics in four Ly α blobs: characterizing the breadth and asymmetry of the [O III] line profile. Note that while we detect an asymmetric wing in some [O III] line profiles, it does not affect the line centroid, which is essential in determining the systemic velocity in the first technique above.

3.5.1. Ly α – [O III] offset

We compare the peak of each Ly α profile with the center of a non-resonant nebular emission line, particularly [O III]. Throughout the paper, the Ly α –H α and Ly α –[O III] offsets are used interchangeably to represent the Ly α offset from the systemic velocity: $\Delta v_{\text{Ly}\alpha}$. Figure 5 shows eight Ly α profiles from this work and from Yang et al. (2011), plotted with increasing $\Delta v_{\text{Ly}\alpha}$.

Because Ly α spectra are somewhat noisy because of the small spectral dispersion ($20\text{--}30\text{ km s}^{-1}$ per pixel), we measure $\Delta v_{\text{Ly}\alpha}$ using the following two methods. First, we measure the velocity of the Ly α peak after smoothing the spectra with a Gaussian filter with FWHM = 90 km s^{-1} , corresponding to our velocity resolution. Second, we fit the red peaks with an asymmetric Gaussian function, which consists of two Gaussian functions with different FWHMs being joined at the center. The two measurements agree to within $\sim 50\text{ km s}^{-1}$, except for CDFS-LAB06 where the second method gives $\Delta v_{\text{Ly}\alpha} = 120\text{ km s}^{-1}$ compared to 320 km s^{-1} from simple smoothing due to the very sharp edge at the blue side of Ly α profile. We adopt the second measurements in this paper and show these fits in Figure 5 and Table 2. None of the conclusions in this paper are affected by this choice.

Figure 6 shows the distribution of $\Delta v_{\text{Ly}\alpha}$ of the eight Ly α blob galaxies in comparison with 41 LBGs (Steidel et al. 2010). Because the spectral resolutions of our Ly α spectra obtained from VLT/X-shooter and Magellan/MagE are higher than those of the Ly α profiles of the LBGs (FWHM $\simeq 370\text{ km s}^{-1}$), we test if the different spectral resolutions affect the Ly α blob–LBG comparison. We repeat the measurement of $\Delta v_{\text{Ly}\alpha}$ after convolving our Ly α profiles to the spectral resolution of LBG sample.

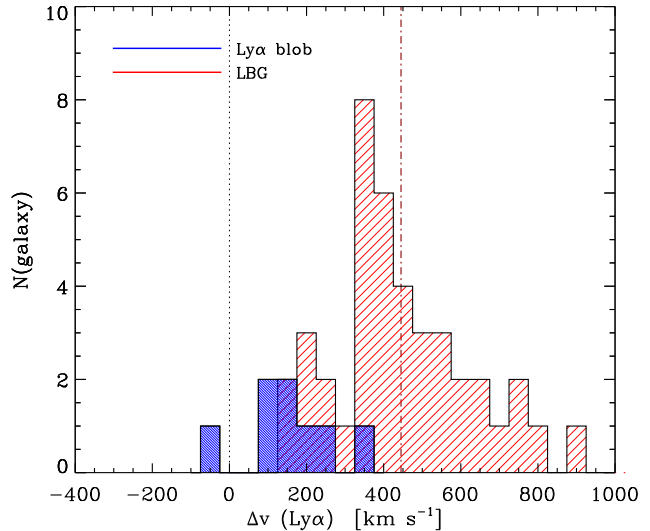


Figure 6. Distribution of $\Delta v_{\text{Ly}\alpha}$ for eight Ly α blob galaxies in comparison to those of 41 LBGs (Steidel et al. 2010). The vertical dot-dashed line indicates the average of LBG sample, $\langle \Delta v_{\text{Ly}\alpha} \rangle = 455\text{ km s}^{-1}$. The $\Delta v_{\text{Ly}\alpha}$ offsets for blob galaxies are generally smaller than those of LBGs. If $\Delta v_{\text{Ly}\alpha}$ is a proxy for the outflow velocity of neutral material, the outflow speeds in Ly α blobs are smaller than for typical star-forming galaxies at $z = 2 - 3$.

The $\Delta v_{\text{Ly}\alpha}$ values change by a negligible amount (only $\pm 50\text{ km s}^{-1}$) except for CDFS-LAB02, where $\Delta v_{\text{Ly}\alpha}$ increases by $+100\text{ km s}^{-1}$ because of its sharp red peak. Therefore, we conclude that the $\Delta v_{\text{Ly}\alpha}$ distributions of Ly α blobs and LBGs can be compared directly.

The $\Delta v_{\text{Ly}\alpha}$ distribution for galaxies within our Ly α blobs reveals smaller velocity offsets than typical of LBGs, confirming previous claims (Yang et al. 2011, see also McLinden et al. 2013). Galaxies within blobs have $\Delta v_{\text{Ly}\alpha} = -60 \rightarrow +400\text{ km s}^{-1}$ with an average of $\langle \Delta v_{\text{Ly}\alpha} \rangle = 160\text{ km s}^{-1}$, while LBGs at similar redshifts have $\Delta v_{\text{Ly}\alpha} = 250 - 900\text{ km s}^{-1}$ with $\langle \Delta v_{\text{Ly}\alpha} \rangle = 445\text{ km s}^{-1}$.

The remaining question is how to interpret these small $\Delta v_{\text{Ly}\alpha}$ values. Two possibilities are: (1) $\Delta v_{\text{Ly}\alpha}$ is a proxy for the gas outflow velocity (v_{exp}), suggesting that the outflows here are weaker than in other star-forming galaxies at $z = 2\text{--}3$ (Verhamme et al. 2006), or (2) there is less neutral gas close to the systemic velocity of the embedded galaxies (Steidel et al. 2010), and $\Delta v_{\text{Ly}\alpha}$ is independent of the outflow speed. We discussed the caveats associated with interpreting $\Delta v_{\text{Ly}\alpha}$ in Yang et al. (2011) and revisit this issue in §4.2.

In the direction of the embedded galaxies, we do not find any Ly α profile that is blue-peak dominated, i.e., $\Delta v_{\text{Ly}\alpha} < 0\text{ km s}^{-1}$. Therefore, there is no evidence along these lines-of-sight for infalling gas (but see §3.7). While the statistics are still small, we place an upper limit on the covering factor of infalling gas (if any) detectable with the $\Delta v_{\text{Ly}\alpha}$ technique. Here the covering factor of any inflowing streams like those predicted by cold-mode accretion (Kereš et al. 2005, 2009; Dekel et al. 2009) must be less than $\sim 13\%$ ($1/8$). We further discuss the covering factor of cold streams in §4.1.

3.5.2. Interstellar Metal Absorption Lines

While strong emission lines such as $\text{Ly}\alpha$ and $[\text{O III}]$ are relatively easy to detect, interstellar metal absorption lines provide a less ambiguous way to measure the outflow velocity of neutral gas lying *in front of* the galaxies targeted with our spectroscopic slit. However, due to the faint UV continuum ($B = 23.8\text{--}26.5$ mag) of our targets, even 8-m telescope struggles to detect their continuum for absorption line studies. Therefore, we obtain higher-S/N absorption line profiles by stacking several lines in each galaxy. Our aim is to test the mild outflow interpretation of our $\Delta v_{\text{Ly}\alpha}$ results by comparing the velocity offset of the stacked ISM absorption profile to the systemic velocity of the galaxy: Δv_{IS} .

Among the six $\text{Ly}\alpha$ blobs, only the UV continua of the galaxies in CDFS-LAB07 and CDFS-LAB14 have S/N higher than 1.5 per spectral pixel ($\sim 20\text{--}30 \text{ km s}^{-1}$), allowing us to marginally extract the absorption profiles. Figure 7(top) shows the rest-frame UV spectra of these two galaxies in comparison with the LBG composite (Shapley et al. 2003). For comparison, we also show the boxcar-smoothed spectra over 20 pixels, corresponding to a velocity width of $450\text{--}600 \text{ km s}^{-1}$. While it is difficult to identify the absorption lines in the un-binned spectra, the smoothed spectra show a good match to the composite spectrum, revealing several low- and high-ionization lines.

As suggested above, it is still difficult to measure individual absorption line profiles, so we stack the five low-ionization lines: Si II $\lambda 1260$, O I $\lambda 1302$, C II $\lambda 1334$, Si II $\lambda 1526$, Al II $\lambda 1670$ to increase the S/N. We do not include the C IV and Si IV lines in the stacking, as these high ionization lines are contaminated with broader absorption features arising from stellar winds from massive stars (Shapley et al. 2003), which are hard to remove in our low S/N spectra. Furthermore, it is possible that these high ionization lines trace different state of gas, while the low ionization lines show similar profiles (Steidel et al. 2010). In Figure 7(bottom), we show the stacked absorption profiles for three galaxies, including the re-analyzed CDFS-LAB02 spectrum that we obtained earlier with Magellan/MagE (Yang et al. 2011).

The stacked absorption profiles here are consistent with weaker outflows than required by the super/hyperwind hypothesis for $\text{Ly}\alpha$ blob emission (Taniguchi & Shioya 2000). These profiles are also consistent with the interpretation of small $\Delta v_{\text{Ly}\alpha}$ indicating small outflow speed, as discussed in §3.5.1. In two galaxies (within CDFS-LAB02 and 07), the absorption profiles have minima around -200 km s^{-1} and might extend up to -500 km s^{-1} , although the exact end of the profile is uncertain due to the low S/N. The shapes of these two absorption profiles are similar to those of typical star-forming galaxies (i.e., LBGs) at the same epoch (Steidel et al. 2010), and the implied outflow velocities are comparable to or slower than in the LBGs. By fitting a Gaussian profile, we obtain $\Delta v_{\text{IS}} = -177 \pm 31 \text{ km s}^{-1}$ and $-236 \pm 31 \text{ km s}^{-1}$ for CDFS-LAB02 and CDFS-LAB07, respectively. We do not find any redshifted absorption component, which is consistent with the absence of any blueshifted $\text{Ly}\alpha$ emission line associated with these galaxies.

In contrast, the profile of CDFS-LAB14's galaxy has

a minimum at $v \simeq 0 \text{ km s}^{-1}$ ($\Delta v_{\text{IS}} = -59 \pm 32 \text{ km s}^{-1}$) without any significant blueshifted (outflowing) component. While the other two profiles terminate roughly at $v \simeq 0 \text{ km s}^{-1}$, CDFS-LAB14's profile extends to $v > 0 \text{ km s}^{-1}$. Thus, its ISM absorption and $\text{Ly}\alpha$ profiles are both consistent with the simple RT model expectation that a symmetric, double-peaked $\text{Ly}\alpha$ profile should emerge from static gas or the absence of bulk motions. Furthermore, the absorption profile is almost saturated, indicating that the column density in this $\text{Ly}\alpha$ blob could be higher than for the other two systems. We will place a constraint on the H I column density of its $\text{Ly}\alpha$ -emitting gas in §3.6.

For CDFS-LAB14, the location of the dip between the blue and red $\text{Ly}\alpha$ velocity peaks changes little for the two extraction apertures shown in Figure 4: one along the line of sight toward the embedded galaxy (the $[\text{O III}]$ source) and the other encompassing the spatially extended gas around $\Delta\theta = -0.5''$. Note that such a trough between $\text{Ly}\alpha$ peaks is often interpreted as arising from absorption by the neutral media between the $\text{Ly}\alpha$ source and observers. For example, Wilman et al. (2005) claim that their IFU spectra of a $\text{Ly}\alpha$ blob (SSA22-LAB02; Steidel blob 2) suggest that the $\text{Ly}\alpha$ emission is absorbed by a foreground slab of neutral gas swept out by a galactic scale outflow. More recently, Martin et al. (2014) show instead that the absorption troughs in the $\text{Ly}\alpha$ emission are actually located at the systemic velocity determined by the $[\text{O III}]$ emission line, i.e., there are negligible velocity offsets between any foreground screen and the systemic velocity. CDFS-LAB14 also demonstrates that a coherent velocity trough, at least over a $\sim 10 \text{ kpc}$ scale, can arise entirely from complicated radiative transfer effects even if there are no significant bulk motions in the $\text{Ly}\alpha$ -emitting gas.

3.5.3. Broadening and Asymmetry in $[\text{O III}]$ Profile

The central galaxies in four $\text{Ly}\alpha$ blobs (CDFS-LAB06, 07, 13, 14) show a broad and/or shifted underlying component to the $[\text{O III}]$ profile, which provides additional constraints on the kinematics of warm ionized gas in the vicinity of the galaxies. To the authors' knowledge, this is the first detection of broadened, asymmetric $[\text{O III}]$ profiles from narrowband-selected $\text{Ly}\alpha$ -emitting galaxies at high redshifts, demonstrating that high spectral resolution is required to fully exploit the NIR spectroscopy of $\text{Ly}\alpha$ galaxies.

We emphasize again that these broad underlying components, even when shifted in velocity, do not affect our measurements of $[\text{O III}]$ line centers, because the $[\text{O III}]$ flux density at the core is dominated by the narrower component, which is likely to arise from nebular regions in the embedded galaxy. As discussed previously, the line centers determined from other non-resonant emission lines (e.g., $\text{H}\alpha$ and $\text{H}\beta$) agree to within $\sim 10 \text{ km s}^{-1}$. Therefore, our measurements of systemic velocity, critical for determining $\Delta v_{\text{Ly}\alpha}$ and Δv_{IS} , remain unchanged.

In Figure 8, we show close-ups of the $[\text{O III}]$ profiles. In CDFS-LAB11, which has the narrowest and the most symmetric $\text{Ly}\alpha$ profile, the $[\text{O III}]$ line is also symmetric. CDFS-LAB10 is excluded from the following analysis because its $[\text{O III}]$ line is elongated in position-velocity space, suggesting some velocity shear, and the neighboring galaxy (CDFS-LAB10A) makes it difficult to reli-

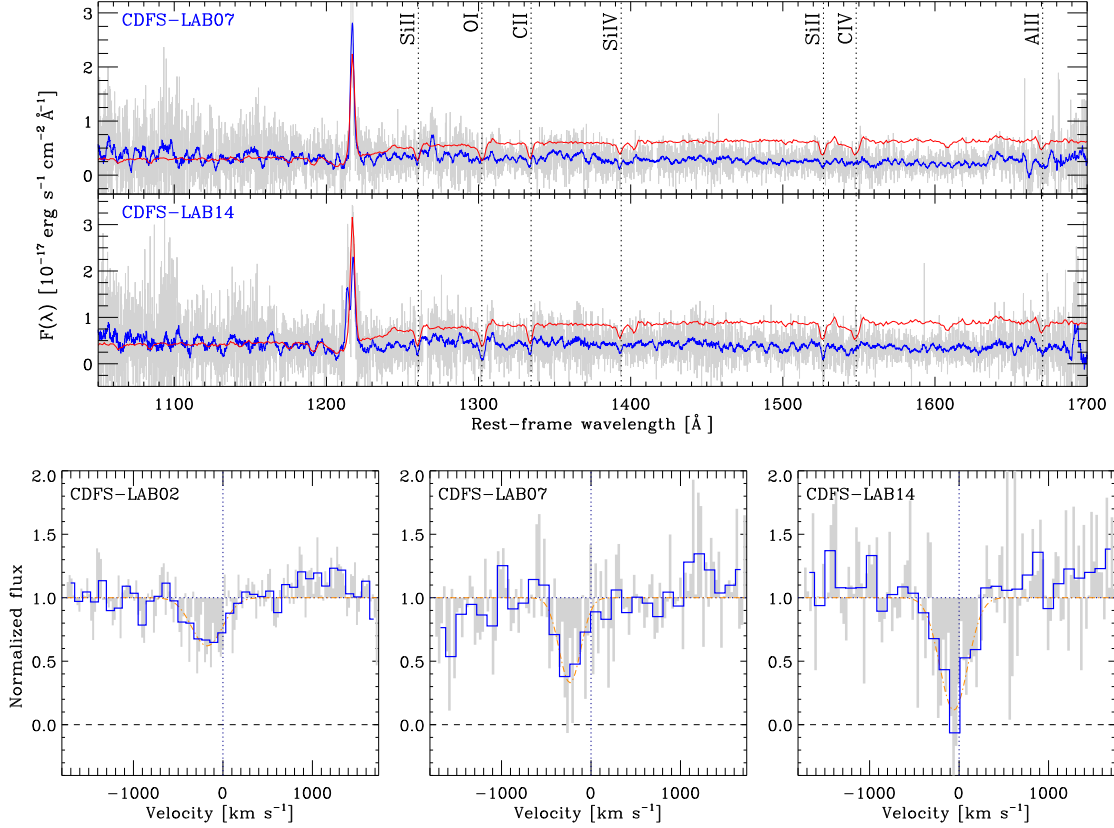


Figure 7. (Top) Rest-frame UV spectra of two embedded blob galaxies with $S/N \gtrsim 1.5 \text{ pixel}^{-1}$ (CDFS-LAB07 and 14). The noisy gray lines show the unbinned spectra, and the thick (blue) solid lines represent the boxcar-smoothed spectra with $\sim 500 \text{ km s}^{-1}$. The thin (red) lines indicate the LBG composite spectrum (Shapley et al. 2003), showing that several absorption lines are detected in these two galaxies. (Bottom) The stacked absorption profiles for three galaxies including CDFS-LAB02, which we have previously studied (Yang et al. 2011), and the two above. The velocity is relative to the systemic velocities determined from the [O III] or $H\alpha$ lines. For each galaxy, we stack five low-ionization lines (two Si II, O I, C II, Al II) to boost the S/N. The gray and blue lines are the unbinned spectra and the spectra binned over 4 pixels, respectively. The orange dot-dashed lines are the Gaussian fits. Two galaxies (CDFS-LAB02 and 07) have small outflow velocities around $\Delta v_{\text{IS}} = -177 \pm 31 \text{ km s}^{-1}$ and $-236 \pm 31 \text{ km s}^{-1}$, respectively. The profiles may extend up to -500 km s^{-1} , but there is no sign of strong outflows ($\sim 1000 \text{ km s}^{-1}$). The absorption profile of another galaxy (CDFS-LAB14) is symmetric around $v \sim 0 \text{ km s}^{-1}$ ($\Delta v_{\text{IS}} = -59 \pm 32 \text{ km s}^{-1}$), suggesting no significant bulk motion. Therefore, at least for three galaxies that have $\text{Ly}\alpha$, [O III] or $H\alpha$, and ISM absorption profiles, there is no fast ($\sim 1000 \text{ km s}^{-1}$) outflowing material along the line-of-sight, which excludes the super/hyperwind model (Taniguchi & Shioya 2000) for extended $\text{Ly}\alpha$ emission in $\text{Ly}\alpha$ blobs. The outflows here are similar to or weaker than in LBGs.

ably extract its profile (see §3.7 for more details of this system). In the remaining four $\text{Ly}\alpha$ blobs, the [O III] profile either has an asymmetric wing (CDFS-LAB06, 07, 13) or a symmetric broad component or components (CDFS-LAB14). Note that the CDFS-LAB06 profile in Figure 8 also includes the light from a faint neighbor or clump to the northwest that is slightly blueshifted ($\sim 50 \text{ km s}^{-1}$). Therefore, the somewhat redshifted wing of CDFS-LAB06 is not due to this contamination.

To extract the underlying broad components, we fit the line profiles with two Gaussian functions (the two dot-dashed lines in Figure 8) and list the results in Table 3. In the Appendix, we describe our fitting procedures in detail. We adopt a two-component fit for simplicity and for comparison with previous studies (although we cannot rule out the possibility that the velocity wings consist of multiple small narrow components). The line center of the broad component (v_{broad}) agree with that of the narrow component in CDFS-LAB14, is blueshifted in CDFS-LAB07, and in CDFS-LAB13, and is marginally redshifted in CDFS-LAB06. The widths of the broad components, corrected for the instrumental resolution,

are relatively small: $\sigma_{\text{broad}} = 45 - 120 \text{ km s}^{-1}$ (FWHM = $100 - 280 \text{ km s}^{-1}$), which would not be detected with lower resolution or lower S/N spectra.

To quantify the contribution of the broad components, we measure the “broad-to-narrow ratio” ($F_{\text{broad}}/F_{\text{narrow}}$), which is defined as the ratio of the flux in the broad [O III] emission line to the flux in the narrow component. Because the fluxes in the two Gaussian components are anti-correlated with each other, this ratio has large uncertainties. We also list the “broad flux fraction” (f_{broad}), which is the ratio of the flux in broad emission to the total [O III] flux ($F_{\text{broad}}/F_{\text{total}}$). The broad emission component is significant with $F_{\text{broad}}/F_{\text{narrow}} = 0.4 - 0.8$ constituting 30%–45% of the total [O III] line flux (although the uncertainties are fairly large). The measurements of the underlying components are highly dependent on the S/N of spectra. Due to the low S/N in the K -band, we are not able to reliably measure the broad line components from permitted lines such as $H\alpha$ or $H\beta$, but similar broad wings are also present in the $H\alpha$ profiles of at least two galaxies (CDFS-LAB07 and 14; see Figure 3).

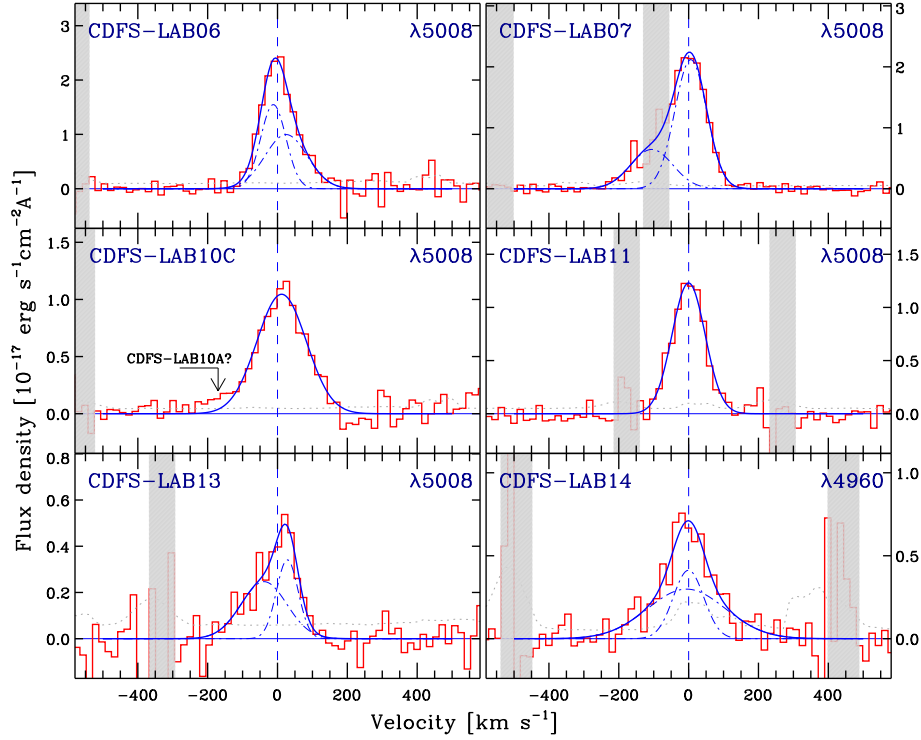


Figure 8. Close up of the $[\text{O III}]$ profiles of six galaxies embedded in $\text{Ly}\alpha$ blobs. The dot-dashed and solid lines indicate the individual Gaussian components and the combined profiles, respectively. Four galaxies (CDFS-LAB06, 07, 13, 14) show a broad component in addition to a narrow component, suggesting a warm, ionized outflow. These broad components are slightly blue or redshifted against the brighter narrow components in three galaxies (CDFS-LAB06, 07 and 13), making the $[\text{O III}]$ lines asymmetric. CDFS-LAB11 shows an almost symmetric single component only. CDFS-LAB10's profile is contaminated by a neighbor. The maximum blueshifted velocity, which ranges from $\Delta v_{\text{max}} = 50$ to 220 km s^{-1} , is smaller than those found in $z \sim 2$ star-forming galaxies ($380 - 1000 \text{ km s}^{-1}$; Genzel et al. 2011), and consistent with our outflow speed estimates from $\Delta v_{\text{Ly}\alpha}$ and the ISM absorption lines.

What is the mechanism responsible for the broad component in the $[\text{O III}]$ profiles? A broad component with a larger line-width (σ_v) of a few hundred km s^{-1} is generally interpreted as a signature of starburst-driven galactic winds, and often observed in local dwarf starbursts (e.g., Westmoquette et al. 2007) and in local ultraluminous infrared galaxies (ULIRGs) (e.g., Soto et al. 2012). While broad components in forbidden lines such as $[\text{O III}]$ are not related to the broad line region (BLR) of Type 1 AGN, they might still arise from the shocked narrow line region (NLR) in AGN. However, the composite spectrum of all of our X-shooter sample has a line ratio $\log([\text{N II}]/\text{H}\alpha) < -0.88$, excluding any significant contribution from AGN (Y. Yang et al. in preparation). Furthermore, in CDFS-LAB11, whose He II and C IV emission lines hint at the presence of an AGN, no broad component is detected.

At high redshift ($z \gtrsim 2$), broadened emission lines were first reported by Shapiro et al. (2009). They found that the stacked spectrum of $z \sim 2$ star-forming galaxies (SFGs) shows broad ($\text{FWHM} \sim 550 \text{ km s}^{-1}$) emission underneath the $\text{H}\alpha + [\text{N II}]$ line complex. More recently, stacked spectra of higher S/N data have revealed that the broad emission is spatially extended over a half-light radius (Newman et al. 2012b). Broad emission lines are now detected from individual SFGs and even from giant star-forming clumps within them (Genzel et al. 2011). Genzel et al. (2011) show that $z \sim 2$ SFGs show broad wings of $\text{H}\alpha$ emission with $\text{FWHM} \sim 300 - 1000 \text{ km s}^{-1}$ ($\sigma_{\text{broad}} \sim 125 - 425$) and employ the maxi-

mum blueshifted velocity, $\Delta v_{\text{max}} = |\langle v_{\text{broad}} \rangle - 2\sigma_{\text{broad}}|$ as a proxy of the outflow speed, finding that SFGs have $\Delta v_{\text{max}} = 380 - 1000 \text{ km s}^{-1}$. Thus, the broad component in these galaxies is attributed to powerful galactic outflows. For compact $\text{Ly}\alpha$ emitters, although there are increasing number of detections of $[\text{O III}]$ and $\text{H}\alpha$ (e.g., McLinden et al. 2011; Finkelstein et al. 2011; Nakajima et al. 2012; Hashimoto et al. 2013), broad emission in $[\text{O III}]$ has not been reported so far, perhaps due to the lower spectral resolution or lower S/N of these studies. Therefore, at the moment, it is not clear whether the broad component and sometime line asymmetry that we observe in $\text{Ly}\alpha$ blobs is a general property of $\text{Ly}\alpha$ -selected galaxies.

As in local ULIRGs and in high redshift SFGs, the detection of a broad component in the $[\text{O III}]$ profile here suggests warm ionized outflows from the galaxies within $\text{Ly}\alpha$ blobs, presumably driven by supernovae and stellar winds. However, while the flux fraction of our broad emission is comparable to those of SFGs, the broad $[\text{O III}]$ wings are narrower ($\sigma_{\text{broad}} = 45 - 120 \text{ km s}^{-1}$) and the inferred velocities much smaller $\Delta v_{\text{max}} = 150 - 260 \text{ km s}^{-1}$. Therefore, at face value, the warm ionized outflows from the $\text{Ly}\alpha$ blob galaxies are not as strong as those in SFGs at similar redshift. Furthermore, these estimates for outflow velocity are roughly consistent with the values obtained from our two other kinematic measures, $\Delta v_{\text{Ly}\alpha}$ and Δv_{IS} (§3.5.1 and §3.5.2), independently discounting shock-heating via super/hyperwinds as a viable powering mechanism.

3.6. Constraint on H I Column Density

Constraining the physical state of the Ly α -emitting gas in a Ly α blob is a critical step to understand its emission mechanism and to directly compare the observations with the numerical simulations (e.g., Faucher-Giguère et al. 2010; Rosdahl & Blaizot 2012; Cen & Zheng 2013; Latif et al. 2011), which predict the Ly α emissivity maps from the gas density, temperature, and UV radiation fields. In this section, as a first step, we estimate the H I column density of a Ly α blob, CDFS-LAB14.

The $\Delta v_{\text{Ly}\alpha}$ and Δv_{IS} analyses of CDFS-LAB14 are consistent with a simple RT model in which the surrounding gas is static or without bulk motions. The third kinematic indicator, the [O III] profile, which suggests a mild outflow, either contradicts the other indicators or is sensitive to gas in a different state (e.g., warm, ionized instead of cold, neutral) or distribution (e.g., around galaxy instead of in galaxy). Here we use the Ly α emission and ISM absorption line profiles to place a constraint on the amount of neutral hydrogen in this Ly α blob. Ultimately, by comparing the Ly α profile with detailed RT models, one could extract a wealth of information, including outflow speed, optical depth, and column density (e.g., Verhamme et al. 2008). We defer such detailed analysis to the future papers and consider the most simple case in this section.

Ly α line transfer in an extremely thick medium of neutral gas has been studied over many decades, and the analytic solutions for simple geometries (like a static homogeneous slab or uniform sphere) are known (Harrington 1973; Neufeld 1990; Dijkstra et al. 2006a). We consider a simple geometry in which a Ly α source is located at the center of a static homogeneous slab with optical depth of τ_0 from the center to the edge. Because Ly α photons generated at the center escape the system through random scattering in the frequency space, the emergent line spectrum is double-peaked profile with its maxima at $\Delta x_{\text{peak}} \equiv (\nu - \nu_0)/\nu_D = \pm 1.173(a\tau_0)^{1/3}$, where x represents the line frequency in units of Doppler width ν_D . a and τ_0 are the Voigt parameter and Ly α optical depth at the line center, respectively (Dijkstra et al. 2006a)⁸. In terms of velocity, the separation between blue and red peaks with same the intensity is

$$\Delta v_{\text{blue-red}} = 424 \text{ km s}^{-1} \cdot \left(\frac{b}{12.85 \text{ km s}^{-1}} \frac{N_{\text{HI}}}{10^{20} \text{ cm}^{-2}} \right)^{1/3}, \quad (1)$$

where b and N_{HI} represent the Doppler parameter ($\sqrt{v_{\text{th}}^2 + v_{\text{turb}}^2}$) and the column density of neutral hydrogen, respectively. If we adopt a uniform sphere geometry instead of a slab, the coefficient of the above equation will decrease to 336 km s^{-1} , and the product ($b N_{\text{HI}}$) will increase by a factor of two for a fixed $\Delta v_{\text{blue-red}}$ value. Note that the blue-to-red peak separation is degenerate between two parameters, b and N_{HI} .

From the Ly α profile of CDFS-LAB14 (Figure 3 and 4), we measure the separation between the blue and red peaks, $\Delta v_{\text{blue-red}} = 790 \pm 39 \text{ km s}^{-1}$. In the analytic solution, the peaks on the blue and red sides of the systemic velocity are each symmetric, whereas for CDFS-LAB14

they are slightly asymmetric. As a result, the RT in this system may require ultimately a more complicated model than the assumed simple geometry.

To constrain N_{HI} , we consider two extreme cases for the Doppler parameter b : First, as a lower limit, $b > 12.85 \text{ km s}^{-1}$, obtained by assuming a temperature $T = 10^4 \text{ K}$ and ignoring the turbulence term. Second, $b < \sigma_{\text{abs}}$, the width of the metal absorption lines. In other words, we assume that the observed velocity width of absorbing material is purely due to the turbulence or random motions inside the slab. The width of the absorption line is $\sigma_{\text{abs}} = 152 \pm 35 \text{ km s}^{-1}$ from a single Gaussian fit (§3.5.2 and Figure 7) and after being corrected for the instrumental line width. For this range of b , we obtain $19.7 < \log N_{\text{HI}} < 20.8$.

Because the Ly α emission is spatially resolved in CDFS-LAB14, we further apply this technique to the extended Ly α -emitting gas in a direction other than toward the embedded galaxy. As shown in Figure 4, the Ly α profile remains double-peaked as we move away from the sight-line directly toward the embedded galaxy. The separation between the blue and red peaks decreases, indicating that $b N_{\text{HI}}$ also decreases. For $\Delta v_{\text{blue-red}} \simeq 650 \text{ km s}^{-1}$, we obtain slightly smaller estimates for the column density: $19.5 < \log N_{\text{HI}} < 20.6$.

Using the accurate measurement of systemic velocity, the metal absorption lines, and the symmetric double-peaked Ly α profile, we are able to place constraints on the N_{HI} toward the galaxy and the extended Ly α -emitting gas, albeit with large uncertainties. It is intriguing that this rough estimate of the H I column density is similar to those of damped Ly α absorption systems (DLA; $N_{\text{HI}} > 2 \times 10^{20} \text{ cm}^{-2}$). While we have identified this Ly α blob by searching for extended Ly α emission, it would be interpreted as a DLA if there were a background QSO whose continuum spectrum showed absorption at the blob redshift. There are similar systems where extended Ly α emission is identified from DLAs very close to the QSO redshift (e.g., Møller et al. 1998; Fynbo et al. 1999; Hennawi et al. 2009).

3.7. Blueshifted Ly α without Broadband Counterpart

Up to this point, we have examined only Ly α emission along the line-of-sight to galaxies embedded in our blobs. In the 2-D spectrum of CDFS-LAB10, however, we identify a region of blueshifted Ly α emission that does not spatially coincide with any of the blob galaxies identified with *HST*. This is the first case in our sample where we detect the Ly α emission from the extended gas itself. Given that a blueshifted Ly α line is a long-sought signature of gas inflows as described in §1 and Figure 1, we present a detailed analysis of CDFS-LAB10 here.

In Figure 9 (bottom), we show the *HST* F606W image of CDFS-LAB10 now rotated and smoothed with a Gaussian kernel to increase the contrast of faint sources. There are three broadband sources labeled CDFS-LAB10A, B, and C within the Ly α contour, which is elongated over $10''$ ($\sim 82 \text{ kpc}$). Figure 9 (top) shows the spatial profiles of the stellar continuum and the emission lines (Ly α and [O III]). The latter are the same as in Figure 4. To obtain the spatial profiles for the continuum, we collapse the 2-D spectra for the rest-frame wavelength range, $[1260\text{\AA}, 1600\text{\AA}]$ and $[4340\text{\AA}, 5400\text{\AA}]$, i.e., redward of Ly α and both sides of the [O III] lines, respectively.

⁸ Note that this coefficient is slightly different from the traditional Neufeld solution (1.066).

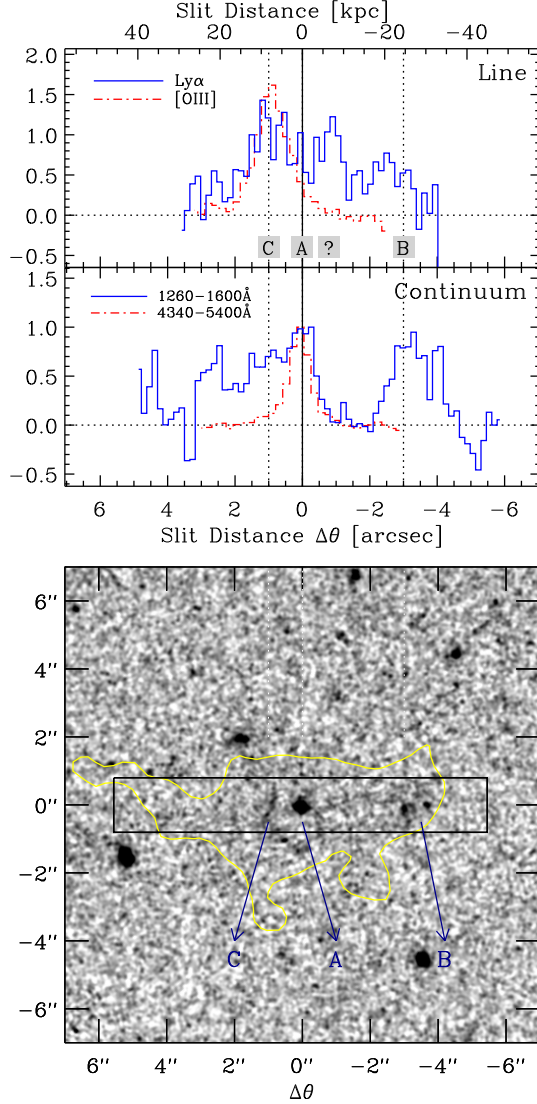


Figure 9. (Top) Spatial profiles of CDFS-LAB10 collapsed in the wavelength direction for the emission lines ($\text{Ly}\alpha$ and $[\text{O III}]$) and the continuum (rest-frame UV and optical), respectively. The upper panel is the same as in Figure 4. The lower panel shows the spatial profiles for the continuum around the $\text{Ly}\alpha$ and $[\text{O III}]$ lines. The solid (blue) and dot-dashed (red) lines represent the profiles obtained from the UVB and NIR arms, respectively. (Bottom) *HST* F606W image of CDFS-LAB10. The yellow contour represents the $\text{Ly}\alpha$. The detected $[\text{O III}]$ emission line originates from a very faint UV source (CDFS-LAB10C; $m_{\text{F606W}} \approx 28$ mag), indicating that extremely deep and high spatial resolution imaging is necessary for identifying possible energy sources for the extended $\text{Ly}\alpha$ emission. There is no counterpart of the $\text{Ly}\alpha$ emission at $\Delta\theta = -1''$ and $\Delta v \sim -500 \text{ km s}^{-1}$ in either the *HST* image or in the X-shooter continuum spectrum (marked by a “?”). Therefore, this isolated $\text{Ly}\alpha$ emission probably arises from the extended gas and represents the first unambiguous detection of a blueshifted $\text{Ly}\alpha$ line with respect to the systemic velocity of a $\text{Ly}\alpha$ blob.

Because of different data reduction modes, the spatial profiles from the NIR arms ($[\text{O III}]$) cover only the central $\sim 6''$, while the profiles from the UVB arm ($\text{Ly}\alpha$) cover $\sim 14''$.

The brightest UV source in the *HST* image, CDFS-LAB10A at the slit center ($\Delta\theta = 0''$), is detected in both the rest-frame UV and optical continua, but not in $\text{Ly}\alpha$ or any strong emission lines ($[\text{O II}]$, $[\text{O III}]$, $\text{H}\beta$, $\text{H}\alpha$). It is still possible that there is a faint $[\text{O III}] \lambda 5007$ line under

a sky line at $\Delta v \sim -550 \text{ km s}^{-1}$ (see Figure 4). Therefore, it is not clear whether galaxy A is at the same redshift as the $\text{Ly}\alpha$ -emitting gas or is a fore- or background galaxy. The galaxy B at $\Delta\theta \sim -3''$ is detected in $\text{Ly}\alpha$, $[\text{O III}]$, and UV continuum and is thus a member of the CDFS-LAB10 blob. Galaxy B’s $\text{Ly}\alpha$ emission is slightly offset from its UV continuum. CDFS-LAB10C, which has a filamentary or elongated morphology in the *HST* image, is the faintest ($m_{\text{F606W}} = 27.9 \pm 0.2$) of the three sources, but the brightest in $\text{Ly}\alpha$ and $[\text{O III}]$. Thus, galaxy C is the dominant source of $\text{Ly}\alpha$ emission from the known galaxies in this $\text{Ly}\alpha$ blob. It appears to be a classic example of an object heavily extinguished in the UV whose $\text{Ly}\alpha$ photons can still escape. Its 2-D $[\text{O III}]$ spectrum shows a velocity shear, suggesting a disk.

There is no obvious counterpart of the $\text{Ly}\alpha$ emission at $\Delta\theta = -1''$ and $\Delta v \sim -500 \text{ km s}^{-1}$ in either the *HST* image or in the X-shooter continuum spectrum. Therefore, this isolated $\text{Ly}\alpha$ emission probably arises from the extended gas. Its line profile is broad, double-peaked, and blueshifted from galaxy B and galaxy C (Figure 4). It is not possible to distinguish whether the bulk motion is inflowing or outflowing (at $\sim 500 \text{ km s}^{-1}$) with respect to galaxy C, the brightest $[\text{O III}]$ source and marker of systemic velocity (Figure 4), because we do not know whether the gas lies in front of or behind galaxy C. This is the first unambiguous detection of a blueshifted $\text{Ly}\alpha$ line with respect to galaxies embedded within $\text{Ly}\alpha$ blobs. It is likely that the blueshift is relative to the systemic velocity of the $\text{Ly}\alpha$ blob as well.

It is not clear what this blueshifted $\text{Ly}\alpha$ emission represents. We consider three possibilities. First, although unlikely, this $\text{Ly}\alpha$ component could be associated with a heavily-extinguished galaxy that lies below the detection limit of the *HST* image ($m_{\text{F606W}} \gg 28$ mag) or with galaxy A, whose redshift is unknown. Second, this gas might be tidally-stripped material arising from a galaxy-galaxy interaction: the two galaxies (B and C) are separated by $\sim 30 \text{ kpc}$ in projected distance and $\sim 200 \text{ km s}^{-1}$ in velocity space. Lastly, but most interestingly, this blueshifted $\text{Ly}\alpha$ emission could be the long-sought, but elusive cold gas accretion along filamentary streams (Kereš et al. 2005, 2009; Dekel et al. 2009).

Note that similarly blueshifted $\text{Ly}\alpha$ emission has been reported in a faint $\text{Ly}\alpha$ emitter at $z = 3.344$, which was discovered in an extremely deep, blind spectroscopic search (Rauch et al. 2011). The spectrum of this peculiar system also has very complex structure (e.g., diffuse fan-like blueshifted $\text{Ly}\alpha$ emission and a DLA system). Rauch et al. (2011) suggest that this blueshifted $\text{Ly}\alpha$ emission can be explained if the gas is inflowing along a filament behind the galaxy and emits fluorescent $\text{Ly}\alpha$ photons induced by the ionizing flux escaping from the galaxy. Discriminating among the above possibilities will require us to further constrain the $\text{Ly}\alpha$ line profile of this blueshifted component and to more fully survey possible member galaxies (or energy sources) within CDFS-LAB10.

Still, we were able to successfully link the $\text{Ly}\alpha$ and $[\text{O III}]$ sources with the embedded galaxies in this complex system and to find blueshifted $\text{Ly}\alpha$ emission that might point to gas inflow. This example raises concerns about how to identify the sources of $\text{Ly}\alpha$ emission and

to interpret the gas morphologies and kinematics solely from Ly α lines. Elongated or filamentary Ly α morphologies may be a sign of bipolar outflows (Matsuda et al. 2004) or related to filamentary cold streams. In CDFS-LAB10, the Ly α spectrum shows two kinematically distinct components around the brightest galaxy A: the upper ($\Delta\theta > 0''$) and lower parts are blue- and redshifted, respectively. In the absence of [O III] spectroscopy, the Ly α data appear to be consistent with either of the above outflow or infalling stream scenarios. However, our detailed analysis including the [O III] line clearly shows that one of the Ly α components arises from the faint galaxy C, which would be difficult to detect without *HST* imaging and is likely the dominant source of Ly α emission. Therefore, we stress that interpreting the Ly α morphology and spectra requires deep high-resolution imaging and the determination of the systemic velocity through NIR spectroscopy.

4. DISCUSSION

4.1. Covering Factor of Inflows and Outflows

Under the assumption that inflowing gas streams (if any) are randomly distributed, and from the non-detection of any blueshifted Ly α -H α or Ly α -[O III] offset in the direction of the eight embedded galaxies tested here (although see Section 3.7), we constrain the covering fraction of inflows to be $< 1/8$ (13%). Likewise, if all of our $\Delta v_{\text{Ly}\alpha}$ offsets are different projections of the same collimated outflow from the galaxies and are a proxy for outflow speed, the covering fraction of *strong* outflows, i.e., super/hyper-winds, is less than $\sim 13\%$.

The covering fraction of gas flows to which we are referring here has a different meaning than often discussed in the literature (e.g., Faucher-Giguère & Kereš 2011; Kimm et al. 2011; Fumagalli et al. 2011). In these theoretical papers, the covering factor is defined as how many sight-lines will be detected in metal or H I *absorption* when bright background sources close to the galaxies are targeted. What we measure in this paper is how often the inflowing gas is aligned with observer's sight-lines so that the column of neutral gas becomes optically thick and blue-shifts Ly α lines against systemic velocity. Nonetheless, Faucher-Giguère & Kereš (2011) predict that the covering factor within the virial radius ($R_{\text{vir}} \simeq 75$ kpc) from their simulated galaxies with a halo mass of $M_h = 3 \times 10^{11} M_\odot$ at $z = 2$ is relatively small: $\sim 3\%$ and 10% for DLAs and Lyman limit systems (LLS), respectively. Within $0.5 \times R_{\text{vir}}$, this factor increases to $\sim 10\%$ and 30% , respectively, and presumably will be much higher directly towards the galaxies (i.e., for a pencil beam or looking down-the-barrel). Note that Faucher-Giguère & Kereš (2011) ignore galactic winds in order to isolate the inflowing streams, so we expect that there will be enough dense material arising from gas accretion to affect the transfer of Ly α photons in our experiments.

What is uncertain is that how the velocity field of this dense material near the galaxy will shift the emerging Ly α profiles and the statistics of $\Delta v_{\text{Ly}\alpha}$, because answering this requires full Ly α radiative transfer treatment. Unlike RT models with simple geometry (e.g., Dijkstra et al. 2006a; Verhamme et al. 2006), cosmological simulations (Faucher-Giguère et al. 2010) predict that the gas inflow can only slightly enhance the blue Ly α peak, im-

plying that the overall profile will be still red-peak dominated if the effects of outflows from the galaxies and IGM absorption are fully considered. Therefore, according to these simulations, our non-detection of infall signatures does not contradict the cold stream model. The Ly α profiles calculated from cold-stream models are in general the integrated profiles of Ly α -emitting gas around the galaxies, which are not detectable by our study. What we need are the predictions for how Ly α profiles are modified and/or shifted against optically-thin lines along the line-of-sight to the galaxies embedded in the extended gas. In this way, the distribution of predicted $\Delta v_{\text{Ly}\alpha}$ can be compared directly with the observations.

It is also critical to take into account the effect of simultaneous outflows and inflows. For example, the H α and [O III] detections suggest that the galaxies embedded in the blobs are forming stars, which could generate mechanical feedback into the surrounding gas cloud. Thus, one might have expected that the innermost part of the gas cloud, close to the galaxies, has galactic scale outflows similar to those of other star-forming galaxies at $z = 2 - 3$ (e.g., Steidel et al. 2010). Gas infall (if any) may dominate at larger radii (up to ~ 50 kpc, the typical blob size). In this case, the emerging Ly α profile will be more sensitive to the core of the Ly α blob, presumably the densest part of the CGM, than to the gas infall. As a result, it might be difficult to detect the infalling gas by measuring $\Delta v_{\text{Ly}\alpha}$. This kind of more realistic, infall+outflow model has not been considered yet in RT calculations, so its spectral signatures are unknown.

4.2. Outflow Speed vs. $\Delta v_{\text{Ly}\alpha}$

In our sample of eight Ly α blobs, the embedded galaxies have smaller velocity offsets ($\langle \Delta v_{\text{Ly}\alpha} \rangle = 160 \text{ km s}^{-1}$) than those of LBGs (445 km s^{-1}). The remaining question is how to interpret these small $\Delta v_{\text{Ly}\alpha}$ values. We consider two possibilities here.

First, if we assume a simple geometry where the outflowing material forms a spherical shell that consists of continuous media, $\Delta v_{\text{Ly}\alpha}$ originates from the resonant scattering of the Ly α photons at the shell as discussed in Verhamme et al. (2008). Note that the emerging Ly α profile is independent of the physical size of the shell as long as the shell have the same outflow velocity. Therefore, this model is applicable to Ly α blobs. In this shell model, a central monochromatic point source is surrounded by an expanding shell of neutral gas with varying column density (N_{HI}) and Doppler b parameter (e.g., Verhamme et al. 2006, 2008). A generic prediction is that the Ly α emission is asymmetric, with the details of the line shape depending on the shell velocity, Doppler parameter b , and optical depth of H I column in the shell. In this simple geometry, the $\Delta v_{\text{Ly}\alpha}$ values can be used as a proxy for outflow velocity of expanding shell, i.e., $v_{\text{exp}} \simeq 0.5 \Delta v_{\text{Ly}\alpha}$. If this is the case, outflow velocities from blob galaxies are much smaller than the values expected from models of strong galactic winds ($\sim 1000 \text{ km s}^{-1}$; Taniguchi & Shioya 2000; Taniguchi et al. 2001; Ohya et al. 2003; Wilman et al. 2005). Furthermore, these offsets are even smaller than the typical Ly α -H α offsets ($250 - 900 \text{ km s}^{-1}$) of LBGs (Steidel et al. 2004, 2010). In particular, while CDFS-LAB14 has the largest $\Delta v_{\text{Ly}\alpha}$ for its red peak, its blue and red peaks have similar intensity, which is a characteristic of a static medium or no bulk

motions (Verhamme et al. 2006; Kollmeier et al. 2010).

Second, in an “expanding bullet” or “clumpy CGM” model (Steidel et al. 2010), the outflowing material, which consists of small individual clumps, has a wide velocity range rather than a single value, and the $\text{Ly}\alpha$ profiles are determined by the Doppler shift that photons acquire when they are last scattered by the clumps just before escaping the system. In this case, the $\text{Ly}\alpha$ – $\text{H}\alpha$ offsets are primarily modulated by the amount of gas that has $v = 0$ component (though it is not clear where this material is spatially located); thus $\Delta v_{\text{Ly}\alpha}$ is not directly correlated with outflow velocity. If this is the case, the small $\Delta v_{\text{Ly}\alpha}$ value of the galaxies in our $\text{Ly}\alpha$ blobs simply indicates that there is less neutral gas at the galaxies’ systemic velocity (presumably near the galaxy) compared to LBGs.

Testing these two hypotheses for $\text{Ly}\alpha$ blobs or LBGs first requires a detailed comparison between high resolution $\text{Ly}\alpha$ profiles and RT predictions. This test is beyond the scope of this paper and will be discussed in the future. As emphasized by Steidel et al. (2010), one also needs to check the consistency of the $\text{Ly}\alpha$ profiles with ISM metal absorption profiles, which depends on high S/N continuum spectra that are not available here. Nonetheless, we attempted such an analysis by stacking many low-ionization absorption lines in three galaxies (section 3.5.2).

For those three embedded galaxies with measured $\Delta v_{\text{Ly}\alpha}$ and Δv_{IS} , the outflow velocity estimates from both methods roughly agree within the uncertainties arising from low S/N and from RT complications. However, closer inspection reveals a discrepancy between the observations and the simplest RT models in that we obtain $\Delta v_{\text{IS}} \sim -200 \text{ km s}^{-1}$ and also $\Delta v_{\text{Ly}\alpha} \sim 200 \text{ km s}^{-1}$ while the RT model with an expanding shell geometry predicts $\Delta v_{\text{IS}} = -v_{\text{exp}} = -0.5 \Delta v_{\text{Ly}\alpha}$. This discrepancy has also appeared in LBGs (Steidel et al. 2010), and Kulas et al. (2012) show that the stacked $\text{Ly}\alpha$ profile of LBGs with double-peaked profiles cannot be reproduced accurately by the shell model. For a wide range of parameters (v_{exp} , b , N_{H}), Kulas et al. (2012) cannot reproduce the location of the red peak, the width of the $\text{Ly}\alpha$ profile, and the metal absorption profile at the same time.

We attribute this discrepancy to the very simple nature of the shell model. By construction or by definition of the expanding “shell”, the internal velocity dispersion of the media that constitute the shell should be much smaller than the expansion velocity of the shell itself, i.e., $v_{\text{exp}}/b \gg 1$. Therefore, one expects that the metal absorption lines arising from this thin shell have very narrow line widths σ_{abs} similar to b , typically \sim tens of km s^{-1} . However, such narrow absorption lines are not observed in either LBGs or $\text{Ly}\alpha$ blobs. Clearly, RT calculations with more realistic geometries and allowing a more thorough comparison with the observed $\text{Ly}\alpha$ profiles are required.

4.3. $\Delta v_{\text{Ly}\alpha}$ in Context of LAEs and LBGs

Given that the galaxies within our $\text{Ly}\alpha$ blobs were selected, by definition, as $\text{Ly}\alpha$ emitters with high equivalent width (EW), the comparison with LAEs suggests that small $\Delta v_{\text{Ly}\alpha}$ values are a general characteristic of all high EW $\text{Ly}\alpha$ -selected populations, be they compact or extended. In addition to this work and Yang et

al. (2011), there are recent studies that measure $\Delta v_{\text{Ly}\alpha}$ for bright compact $\text{Ly}\alpha$ -emitters (McLinden et al. 2011; Finkelstein et al. 2011; Hashimoto et al. 2013; Guaita et al. 2013) and $\text{Ly}\alpha$ blobs (McLinden et al. 2013), which also find small $\text{Ly}\alpha$ –[O III] offsets for LAEs ranging from $35 - 340 \text{ km s}^{-1}$. A Kolmogorov–Smirnov test fails to distinguish the $\Delta v_{\text{Ly}\alpha}$ distribution of our eight $\text{Ly}\alpha$ blobs from that of ten compact LAEs compiled from the four studies mentioned above. Thus, we now have a fairly large sample of high-EW $\text{Ly}\alpha$ emitters (compact or extended) with $\Delta v_{\text{Ly}\alpha} = -60 \rightarrow +400 \text{ km s}^{-1}$, which is clearly different from the distribution for LBGs (see Section 3.5.1).

The smaller $\Delta v_{\text{Ly}\alpha}$ of LAEs and LABs might be related to their higher $\text{Ly}\alpha$ equivalent widths. An anti-correlation between $\text{EW}(\text{Ly}\alpha)$ and $\Delta v_{\text{Ly}\alpha}$ in a compilation of LAE and LBG samples has been suggested (Hashimoto et al. 2013). Even within the LBG population itself there is an indication that $\Delta v_{\text{Ly}\alpha}$ decreases as $\text{EW}(\text{Ly}\alpha)$ increases. Shapley et al. (2003) find an anti-correlation between the $\text{EW}(\text{Ly}\alpha)$ and the velocity offsets between interstellar absorption and $\text{Ly}\alpha$ emission lines, $\Delta v_{\text{Ly}\alpha-\text{abs}}$.⁹ From the stacked spectra of LBGs binned at different $\text{EW}(\text{Ly}\alpha)$, they show that with increasing $\text{Ly}\alpha$ line strength from -15\AA to 53\AA , $\Delta v_{\text{Ly}\alpha-\text{abs}}$ decreases from 800 km s^{-1} to 480 km s^{-1} . Because $\Delta v_{\text{Ly}\alpha-\text{abs}} = \Delta v_{\text{Ly}\alpha} + |\Delta v_{\text{IS}}|$, we can infer that $\Delta v_{\text{Ly}\alpha}$ is likely to decrease as $\text{EW}(\text{Ly}\alpha)$ increases unless the observed anti-correlation is entirely due to $|\Delta v_{\text{IS}}|$.

The origin of the apparent relationship between larger $\text{EW}(\text{Ly}\alpha)$ and smaller $\Delta v_{\text{Ly}\alpha}$ is not understood. It is possible that other physical properties drive this anti-correlation: for example, LBGs tend to have brighter continuum magnitudes, thus likely higher star formation rates and stellar masses, than are of typical LAEs. Hashimoto et al. (2013) propose that low H I column density, and thus a small number of resonant scatterings of $\text{Ly}\alpha$ photons, might be responsible for the strong $\text{Ly}\alpha$ emission and small $\Delta v_{\text{Ly}\alpha}$ of $\text{Ly}\alpha$ emitters.

What we do know from our $\Delta v_{\text{Ly}\alpha}$ measurements is that LAEs and $\text{Ly}\alpha$ blobs are kinematically similar. Therefore, the mystery remains as to what powers $\text{Ly}\alpha$ nebulae, or, in other words, why certain galaxies have more spatially-extended $\text{Ly}\alpha$ gas (i.e., blobs) than others (i.e., compact LAEs) with similar $\Delta v_{\text{Ly}\alpha}$ and $\text{EW}(\text{Ly}\alpha)$. While the answer may be related to photo-ionization from (buried) AGN (e.g., see Section 4.4 or Yang et al. 2014), an extended proto-intracluster medium that can scatter or transport the $\text{Ly}\alpha$ photons out to larger distances, or less dust to destroy $\text{Ly}\alpha$ photons (cf. Hayes et al. 2013), discriminating among these possibilities will require a multi-wavelength analysis of a large sample of $\text{Ly}\alpha$ blobs. For now, the similarity here of LABs and LAEs suggests that differences in gas kinematics are not responsible for the extended $\text{Ly}\alpha$ halos.

4.4. CDFS-LAB11: Photo-ionization by AGN?

From the nearly symmetric $\text{Ly}\alpha$ profile (Fig. 10), C IV and He II detection, and rest-frame optical line ratios, we hypothesize that an AGN in CDFS-LAB11 ionizes the gas surrounding the galaxies, making $\text{Ly}\alpha$ relatively opti-

⁹ The notation, $\Delta v_{\text{em-abs}}$ is used in Shapley et al. (2003).

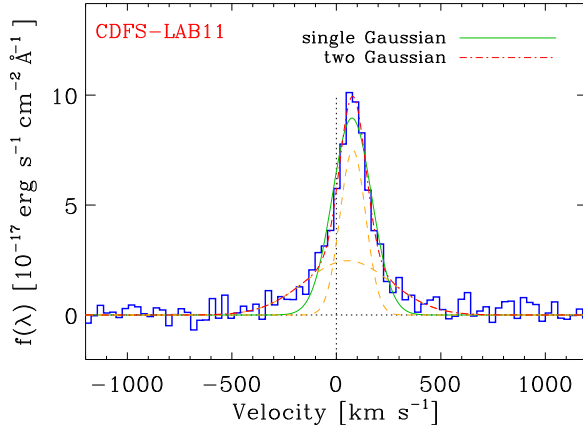


Figure 10. $\text{Ly}\alpha$ profile of CDFS-LAB11. The solid and dot-dashed lines represent the fits with one and two Gaussian components, respectively. The two dashed lines are the narrow and broad components. The narrow component may arise from an AGN that ionizes the gas surrounding the embedded galaxies, making $\text{Ly}\alpha$ relatively optically thin and preventing the resonant scattering of $\text{Ly}\alpha$ photons from dominating the shape of the profile.

cally thin and preventing the resonant scattering of $\text{Ly}\alpha$ photons from dominating the shape of the profile. While fitting the profile requires an underlying broad component ($\text{FWHM} \simeq 480 \text{ km s}^{-1}$), the narrow component (redshifted by $\simeq 80 \text{ km s}^{-1}$) has a small velocity width ($\text{FWHM} \simeq 110 \text{ km s}^{-1}$), comparable to that of the $[\text{O III}]$ line ($\simeq 80 \text{ km s}^{-1}$). Therefore, if we assume that $\text{Ly}\alpha$ and $[\text{O III}]$ photons originate from the same region, resonant scattering by the IGM/CGM does not broaden the intrinsic profile significantly. In other words, at least along our LOS, the optical depth of CDFS-LAB11’s IGM/CGM is smaller than for the other $\text{Ly}\alpha$ blobs in our sample and for typical $\text{Ly}\alpha$ emitters at high redshifts.

A nearly symmetric and narrow $\text{Ly}\alpha$ profile such as CDFS-LAB11’s is rarely observed among high- z $\text{Ly}\alpha$ -emitting galaxies. However, $\text{Ly}\alpha$ radiative transfer calculations show that such $\text{Ly}\alpha$ profiles can be generated in the presence of a central ionizing source. For example, Dijkstra et al. (2006a) investigate the emerging $\text{Ly}\alpha$ profiles from an collapsing/expanding sphere centered on an ionizing source (an AGN) for different luminosities (see their Figures 11 and 12). They find that if the ionizing source is strong and the $\text{Ly}\alpha$ is *relatively* optically thin (line-center optical depth $\tau_0 < 10^3$), the separation of the characteristic double-peaks become smaller ($\Delta v_{\text{blue-red}} \ll 100 \text{ km s}^{-1}$) as the ionizing source gets stronger. The overall profile becomes symmetric, and is blue or redshifted depending on the flow direction, but again by small amount ($\Delta v_{\text{Ly}\alpha} \ll 100 \text{ km s}^{-1}$). These authors were skeptical that the sign of the $\text{Ly}\alpha$ shift and the small $\text{Ly}\alpha$ offset ($\Delta v_{\text{Ly}\alpha} \sim$ a few tens km s^{-1}) from the systemic velocity could be measured. However, with the right strategy (i.e., high spectral resolution and a careful choice of survey redshift), we are able to reliably measure the predicted small offset. Clearly, more detailed comparisons with the RT models are required.

A broad, asymmetric $\text{Ly}\alpha$ profile with a sharp blue edge (e.g., CDFS-LAB06 and 07) is characteristic of high- z $\text{Ly}\alpha$ -emitters. In spectroscopic follow-up observations of $\text{Ly}\alpha$ -emitter candidates, where spectral coverage is limited, these characteristics alone are often used

to discriminate high- z $\text{Ly}\alpha$ emitters from possible low- z interlopers. The example of CDFS-LAB11 demonstrates that caution is required because a narrow and symmetric $\text{Ly}\alpha$ line can also arise when the ISM or CGM of a candidate galaxy is significantly photo-ionized, e.g., by AGN. On the bright side, our $\Delta v_{\text{Ly}\alpha}$ velocity offset technique could be used for studying gas infall or outflow in high- z QSOs instead of relying on only the $\text{Ly}\alpha$ line profile (e.g., Weidinger et al. 2004).

5. CONCLUSIONS

Exploring the origin of $\text{Ly}\alpha$ nebulae (“blobs”) at high redshift requires measurements of their gas kinematics that are difficult with only the resonant, optically-thick $\text{Ly}\alpha$ line. To define gas motions relative to the systemic velocity of the nebula, the $\text{Ly}\alpha$ line must be compared with non-resonant lines, which are not much altered by radiative transfer effects. We made first comparison of non-resonant $\text{H}\alpha \lambda 6563$ to extended $\text{Ly}\alpha$ emission for two bright $\text{Ly}\alpha$ blobs in Yang et al. (2011), concluding that, within the context of a simple radiative transfer model, the gas was static or mildly outflowing at $\lesssim 250 \text{ km s}^{-1}$. However, it was unclear if these two $\text{Ly}\alpha$ blobs, which are the brightest in the sample, are representative of the general $\text{Ly}\alpha$ blob population. Furthermore, geometric effects — infall along filaments or bi-polar outflows — might hide bulk motions of the gas when only viewed from the two directions toward these two $\text{Ly}\alpha$ blobs. With VLT X-shooter, we obtain optical and near-infrared spectra of six additional $\text{Ly}\alpha$ blobs from the Yang et al. (2010) sample. With a total of eight $\text{Ly}\alpha$ blobs, we investigate the gas kinematics within $\text{Ly}\alpha$ blobs using three techniques: the $\text{Ly}\alpha$ offset from the systemic velocity ($\Delta v_{\text{Ly}\alpha}$), the shape and shift (Δv_{IS}) of the ISM metal absorption line profiles, and the breadth of the $[\text{O III}]$ line profile. Our findings are:

1. Both $\text{Ly}\alpha$ and non-resonant lines confirm that these blobs lie at the survey redshift ($z \sim 2.3$). We also detect the $[\text{O II}] \lambda \lambda 3727, 3729$, $[\text{O III}] \lambda 4959$, $[\text{O III}] \lambda 5007$, and $\text{H}\beta \lambda 4861$ lines. All non-resonant line velocities are consistent with each other and with arising from the galaxy or galaxies embedded in the $\text{Ly}\alpha$ blob. $[\text{O III}]$, which is observed at high signal-to-noise in all cases and whose profile is an RT-independent constraint on the gas kinematics, is a particularly good diagnostic line for this redshift and instrument.
2. The majority of the blobs (6/8) have broadened $\text{Ly}\alpha$ profiles indicating radiative transfer effects. These $\text{Ly}\alpha$ profiles are consistent with being in the same family of objects as predicted by RT, with profile shapes ranging from symmetric double-peaked, to asymmetric red peak dominated, to a single red peak. The fraction of double-peaked profiles is $\sim 38\%$ (3/8).
3. The narrow $\text{Ly}\alpha$ profile systems (CDFS-LAB01A, CDFS-LAB11), whose $\text{Ly}\alpha$ profile is not significantly broader than the $[\text{O III}]$ or $\text{H}\alpha$ lines, have the smallest $\Delta v_{\text{Ly}\alpha}$ offsets, the most spatially compact $\text{Ly}\alpha$ emission, and the only C IV and He II lines detected, implying that a hard ionizing source, pos-

sibly an AGN, is responsible for the lower optical depth toward the central embedded galaxies.

4. With a combination of $\Delta v_{\text{Ly}\alpha}$, the interstellar metal absorption line profile, and a new indicator, the spectrally-resolved [O III] line profile, we detect gas moving along the line of sight to galaxies embedded in the $\text{Ly}\alpha$ blob center. Although not all three indicators are available for all $\text{Ly}\alpha$ blobs, the implied speeds and direction are roughly consistent for the sample, suggesting a simple picture in which the gas is stationary or slowly outflowing at a few hundred km s^{-1} from the embedded galaxies. These outflow speeds are similar to those of LAEs, suggesting that outflow speed is not the dominant driver of extended $\text{Ly}\alpha$ emission. Furthermore, these outflow speeds exclude models in which star formation or AGN produce “super” or “hyper” winds of up to $\sim 1000 \text{ km s}^{-1}$ (Taniguchi & Shioya 2000).

More specifically:

- We compare the non-resonant emission lines [O III] and $\text{H}\alpha$ to the $\text{Ly}\alpha$ profile to obtain the velocity offset $\Delta v_{\text{Ly}\alpha}$. The galaxies embedded within our $\text{Ly}\alpha$ blobs have smaller $\Delta v_{\text{Ly}\alpha}$ than those of LBGs, confirming the previous claims (Yang et al. 2011). The galaxies within $\text{Ly}\alpha$ blobs have $\Delta v_{\text{Ly}\alpha} = -60 \rightarrow +400 \text{ km s}^{-1}$ with an average of $\langle \Delta v_{\text{Ly}\alpha} \rangle = 160 \text{ km s}^{-1}$, while LBGs at similar redshifts have $\Delta v_{\text{Ly}\alpha} = 250 - 900 \text{ km s}^{-1}$. The small $\Delta v_{\text{Ly}\alpha}$ in the $\text{Ly}\alpha$ blobs are consistent with those measured for compact LAEs.
- By stacking low-ionization metal absorption lines, we measure the outflow velocity of neutral gas in front of the galaxies in the $\text{Ly}\alpha$ blobs. Galaxies in two $\text{Ly}\alpha$ blobs show an outflow speed of $\sim 250 \text{ km s}^{-1}$, while another has an almost symmetric absorption line profile centered at $\Delta v_{\text{IS}} = 0 \text{ km s}^{-1}$, consistent with no significant bulk motion. The ISM absorption line profiles here have low S/N, but are very roughly consistent with those of some LBGs (at the level of several hundred km s^{-1} outflows).
- The high spectral resolution of our data reveals broad wings in the [O III] profiles of four $\text{Ly}\alpha$ blobs. This new kinematic diagnostic suggests warm ionized outflows driven by supernovae and stellar winds. These broad line components are narrower ($\sigma_{\text{broad}} = 45 - 120 \text{ km s}^{-1}$) and have a maximum blueshifted velocity ($\Delta v_{\text{max}} = 150 - 260 \text{ km s}^{-1}$) smaller than those of $z \sim 2$ star-forming galaxies (SFGs), implying weaker outflows here than for LBGs and SFGs at similar redshifts.
- If we assume that the detected outflows are different projections of the same outflow from the $\text{Ly}\alpha$ blob center, we can estimate the effects of flow geometry on our measurements given that our large sample size allows averaging over many lines-of-sight. The absence of any strong ($\sim 1000 \text{ km s}^{-1}$) outflows among the eight galaxies tested is not a

projection effect: their covering fraction is $< 1/8$ (13%). Likewise, the lack of a blue-peak dominated $\text{Ly}\alpha$ profile, at least in the direction of the embedded galaxies (see point 6. below), implies that the covering factor of any cold streams (Kereš et al. 2005, 2009; Dekel et al. 2009) is less than 13%. The channeling of gravitational cooling radiation into $\text{Ly}\alpha$ may not be significant over the radii probed by our techniques here.

5. Constraining the physical state of $\text{Ly}\alpha$ -emitting gas in a $\text{Ly}\alpha$ blob is a critical step in understanding its emission mechanism and in comparing to simulations. For one $\text{Ly}\alpha$ blob whose $\text{Ly}\alpha$ profile and ISM metal absorption lines suggest no significant bulk motion (CDFS-LAB14), at least in its cool and neutral gas, we assume a simple RT model and make the first column density measurement of gas in a embedded galaxy, finding that it is consistent with a DLA.
6. For one peculiar system (CDFS-LAB10), we discover blueshifted $\text{Ly}\alpha$ emission that is *not* directly associated with any embedded galaxy. This $\text{Ly}\alpha$ emitting gas is blueshifted relative to two embedded galaxies, suggesting that it arose from a tidal interaction between the galaxies or is actually flowing into the blob center. The former is expected in these overdense regions, where *HST* images resolve many galaxies. The latter might signify the predicted but elusive cold gas accretion along filaments.

We thank the anonymous referee for her or his thorough reading of the manuscript and helpful comments. The authors thank Daniel Eisenstein for his contributions at the start of this project. We thank Jason X. Prochaska for helpful discussions. YY thanks the MPIA ENIGMA group for the helpful discussions. YY also thanks the Theoretical Astrophysics Center at the University of California, Berkeley for the travel support, as well as Claude-André Faucher-Giguère, Dušan Kereš and Daniel Kasen for the helpful discussions during that stay. YY also thanks Sangeeta Malhotra for a helpful discussion regarding the LAE and LBG connection. YY acknowledges support from the BMBF/DLR grant Nr. 50 OR 1306. A.I.Z. thanks the Max-Planck-Institut für Astronomie and the Center for Cosmology and Particle Physics at New York University for their hospitality and support during her stays there. A.I.Z. acknowledges support from the NSF Astronomy and Astrophysics Research Program through grant AST-0908280 and from the NASA Astrophysics Data Analysis Program through grant NNX10AD47G. She also thank the generosity of the John Simon Guggenheim Memorial Foundation.

Facilities: VLT (X-shooter, SINFONI), Magellan (MagE)

REFERENCES

- Bland, J., & Tully, B. 1988, *Nature*, 334, 43
 Cen, R., & Zheng, Z. 2013, *ApJ*, 775, 112

- Colbert, J. W., Teplitz, H., Francis, P., Palunas, P., Williger, G. M., & Woodgate, B. 2006, *ApJ*, 637, L89
- Damen, M., Labbé, I., van Dokkum, P. G., et al. 2011, *ApJ*, 727, 1
- Dekel, A., et al. 2009, *Nature*, 457, 451
- Dey, A., et al. 2005, *ApJ*, 629, 654
- Dijkstra, M., Haiman, Z., & Spaans, M. 2006, *ApJ*, 649, 14
- Dijkstra, M., Haiman, Z., & Spaans, M. 2006, *ApJ*, 649, 37
- Dijkstra, M., & Loeb, A. 2009, *MNRAS*, 400, 1109
- Erb, D. K., Bogosavljević, M., & Steidel, C. C. 2011, *ApJ*, 740, L31
- Fardal, M. A., Katz, N., Gardner, J. P., Hernquist, L., Weinberg, D. H., & Davé, R. 2001, *ApJ*, 562, 605
- Faucher-Giguère, C.-A., Kereš, D., Dijkstra, M., Hernquist, L., & Zaldarriaga, M. 2010, *ApJ*, 725, 633
- Faucher-Giguère, C.-A., & Kereš, D. 2011, *MNRAS*, 412, L118
- Finkelstein, S. L., Hill, G. J., Gebhardt, K., et al. 2011, *ApJ*, 729, 140
- Foreman-Mackey, D., Hogg, D. W., Lang, D., & Goodman, J. 2013, *PASP*, 125, 306
- Francis, P. J., et al. 2001, *ApJ*, 554, 1001
- Fumagalli, M., Prochaska, J. X., Kasen, D., et al. 2011, *MNRAS*, 418, 1796
- Fynbo, J. U., Møller, P., & Warren, S. J. 1999, *MNRAS*, 305, 849
- Gawiser, E., et al. 2006, *ApJS*, 162, 1
- Geach, J. E., et al. 2009, *ApJ*, 700, 1
- Genzel, R., Newman, S., Jones, T., et al. 2011, *ApJ*, 733, 101
- Goerdt, T., Dekel, A., Sternberg, A., Ceverino, D., Teyssier, R., & Primack, J. R. 2010, *MNRAS*, 933
- Guaita, L., Francke, H., Gawiser, E., et al. 2013, *A&A*, 551, A93
- Haiman, Z., & Rees, M. J. 2001, *ApJ*, 556, 87
- Haiman, Z., Spaans, M., & Quataert, E. 2000, *ApJ*, 537, L5
- Harrington, J. P. 1973, *MNRAS*, 162, 43
- Hashimoto, T., Ouchi, M., Shimasaku, K., et al. 2013, *ApJ*, 765, 70
- Hayes, M., Scarlata, C., & Siana, B. 2011, *Nature*, 476, 304
- Hayes, M., Östlin, G., Schaerer, D., et al. 2013, *ApJ*, 765, L27
- Hennawi, J. F., Prochaska, J. X., Kollmeier, J., & Zheng, Z. 2009, *ApJ*, 693, L49
- Keel, W. C., Cohen, S. H., Windhorst, R. A., & Waddington, I. 1999, *AJ*, 118, 2547
- Kelson, D. D. 2003, *PASP*, 115, 688
- Kereš, D., Katz, N., Weinberg, D. H., & Davé, R. 2005, *MNRAS*, 363, 2
- Kereš, D., Katz, N., Fardal, M., Davé, R., & Weinberg, D. H. 2009, *MNRAS*, 395, 160
- Kimm, T., Slyz, A., Devriendt, J., & Pichon, C. 2011, *MNRAS*, 413, L51
- Kollmeier, J. A., Zheng, Z., Davé, R., Gould, A., Katz, N., Miralda-Escudé, J., & Weinberg, D. H. 2010, *ApJ*, 708, 1048
- Kulas, K. R., Shapley, A. E., Kollmeier, J. A., et al. 2012, *ApJ*, 745, 33
- Latif, M. A., Schleicher, D. R. G., Spaans, M., & Zaroubi, S. 2011, *MNRAS*, 413, L33
- Lehmer, B. D., Brandt, W. N., Alexander, D. M., et al. 2005, *ApJS*, 161, 21
- Luo, B., Bauer, F. E., Brandt, W. N., et al. 2008, *ApJS*, 179, 19
- Martin, D. C., Chang, D., Matuszewski, M., et al. 2014, *arXiv:1402.4809*
- Matsuda, Y., et al. 2004, *AJ*, 128, 569
- Matsuda, Y., Yamada, T., Hayashino, T., Yamauchi, R., & Nakamura, Y. 2006, *ApJ*, 640, L123
- Matsuda, Y., Yamada, T., Hayashino, T., et al. 2011, *MNRAS*, 410, L13
- McLinden, E. M., Finkelstein, S. L., Rhoads, J. E., et al. 2011, *ApJ*, 730, 136
- McLinden, E. M., Malhotra, S., Rhoads, J. E., et al. 2013, *ApJ*, 767, 48
- Møller, P., Warren, S. J., & Fynbo, J. U. 1998, *A&A*, 330, 19
- Nakajima, K., Ouchi, M., Shimasaku, K., et al. 2012, *ApJ*, 745, 12
- Neufeld, D. A. 1990, *ApJ*, 350, 216
- Newman, S. F., Genzel, R., Förster-Schreiber, N. M., et al. 2012, *ApJ*, 761, 43
- Nilsson, K. K., Fynbo, J. P. U., Møller, P., Sommer-Larsen, J., & Ledoux, C. 2006, *A&A*, 452, L23
- Ohyama, Y., et al. 2003, *ApJ*, 591, L9
- Ouchi, M., et al. 2009, *ApJ*, 696, 1164
- Prescott, M. K. M., Kashikawa, N., Dey, A., & Matsuda, Y. 2008, *ApJ*, 678, L77
- Prescott, M. K. M., Dey, A., & Jannuzi, B. T. 2009, *ApJ*, 702, 554
- Prescott, M. K. M., Dey, A., & Jannuzi, B. T. 2012, *ApJ*, 748, 125
- Prescott, M. K. M., Dey, A., Brodwin, M., et al. 2012, *ApJ*, 752, 86
- Rauch, M., Becker, G. D., Haehnelt, M. G., et al. 2011, *MNRAS*, 418, 1115
- Rix, H.-W., et al. 2004, *ApJS*, 152, 163
- Rosdahl, J., & Blaizot, J. 2012, *MNRAS*, 423, 344
- Saito, T., Shimasaku, K., Okamura, S., Ouchi, M., Akiyama, M., & Yoshida, M. 2006, *ApJ*, 648, 54
- Saito, T., Shimasaku, K., Okamura, S., Ouchi, M., Akiyama, M., Yoshida, M., & Ueda, Y. 2008, *ApJ*, 675, 1076
- Scarlata, C., et al. 2009, *ApJ*, 706, 1241
- Schaerer, D., & Verhamme, A. 2008, *A&A*, 480, 369
- Shapiro, K. L., Genzel, R., Quataert, E., et al. 2009, *ApJ*, 701, 955
- Shapley, A. E., Steidel, C. C., Pettini, M., & Adelberger, K. L. 2003, *ApJ*, 588, 65
- Smith, D. J. B., & Jarvis, M. J. 2007, *MNRAS*, 378, L49
- Soto, K. T., Martin, C. L., Prescott, M. K. M., & Armus, L. 2012, *ApJ*, 757, 86
- Steidel, C. C., Adelberger, K. L., Shapley, A. E., Pettini, M., Dickinson, M., & Giavalisco, M. 2000, *ApJ*, 532, 170
- Steidel, C. C., Shapley, A. E., Pettini, M., Adelberger, K. L., Erb, D. K., Reddy, N. A., & Hunt, M. P. 2004, *ApJ*, 604, 534
- Steidel, C. C., Erb, D. K., Shapley, A. E., et al. 2010, *ApJ*, 717, 289
- Taniguchi, Y., Shioya, Y., & Kakazu, Y. 2001, *ApJ*, 562, L15
- Taniguchi, Y., & Shioya, Y. 2000, *ApJ*, 532, L13
- Verhamme, A., Schaerer, D., & Maselli, A. 2006, *A&A*, 460, 397
- Verhamme, A., Schaerer, D., Atek, H., & Tapken, C. 2008, *A&A*, 491, 89
- Vernet, J., Dekker, H., D’Odorico, S., et al. 2011, *A&A*, 536, A105
- Weidinger, M., Møller, P., & Fynbo, J. P. U. 2004, *Nature*, 430, 999
- Weijmans, A.-M., Bower, R. G., Geach, J. E., et al. 2010, *MNRAS*, 402, 2245
- Westmoquette, M. S., Exter, K. M., Smith, L. J., & Gallagher, J. S. 2007, *MNRAS*, 381, 894
- Wilman, R. J., Gerssen, J., Bower, R. G., Morris, S. L., Bacon, R., de Zeeuw, P. T., & Davies, R. L. 2005, *Nature*, 436, 227
- Yamada, T., Matsuda, Y., Kousai, K., et al. 2012, *ApJ*, 751, 29
- Yang, Y., Zabludoff, A., Tremonti, C., Eisenstein, D., & Davé, R. 2009, *ApJ*, 693, 1579
- Yang, Y., Zabludoff, A., Eisenstein, D., & Davé, R. 2010, *ApJ*, 719, 1654
- Yang, Y., Zabludoff, A., Jahnke, K., et al. 2011, *ApJ*, 735, 87
- Yang, Y., Walter, F., Decarli, R., et al. 2014, *ApJ*, 784, 171

APPENDIX

DECOMPOSITION OF [O III] PROFILES

To test if two velocity components are needed to fit our spectrally-resolved [O III] profiles and to extract the line parameters, we employ the [O III] profiles with two Gaussian functions using a Markov Chain Monte Carlo (MCMC) technique. We use the *emcee* software (Foreman-Mackey et al. 2013) to sample the distributions of six parameters: line center, width, and fluxes for the two Gaussian profiles. We require that (1) the line widths of both components are larger than the instrumental line width (31 km s^{-1} ; the vertical dotted lines in Figure 11), (2) the peak of each component should be at least 5% of the observed peak intensity, and (3) the peak of the narrow component is higher

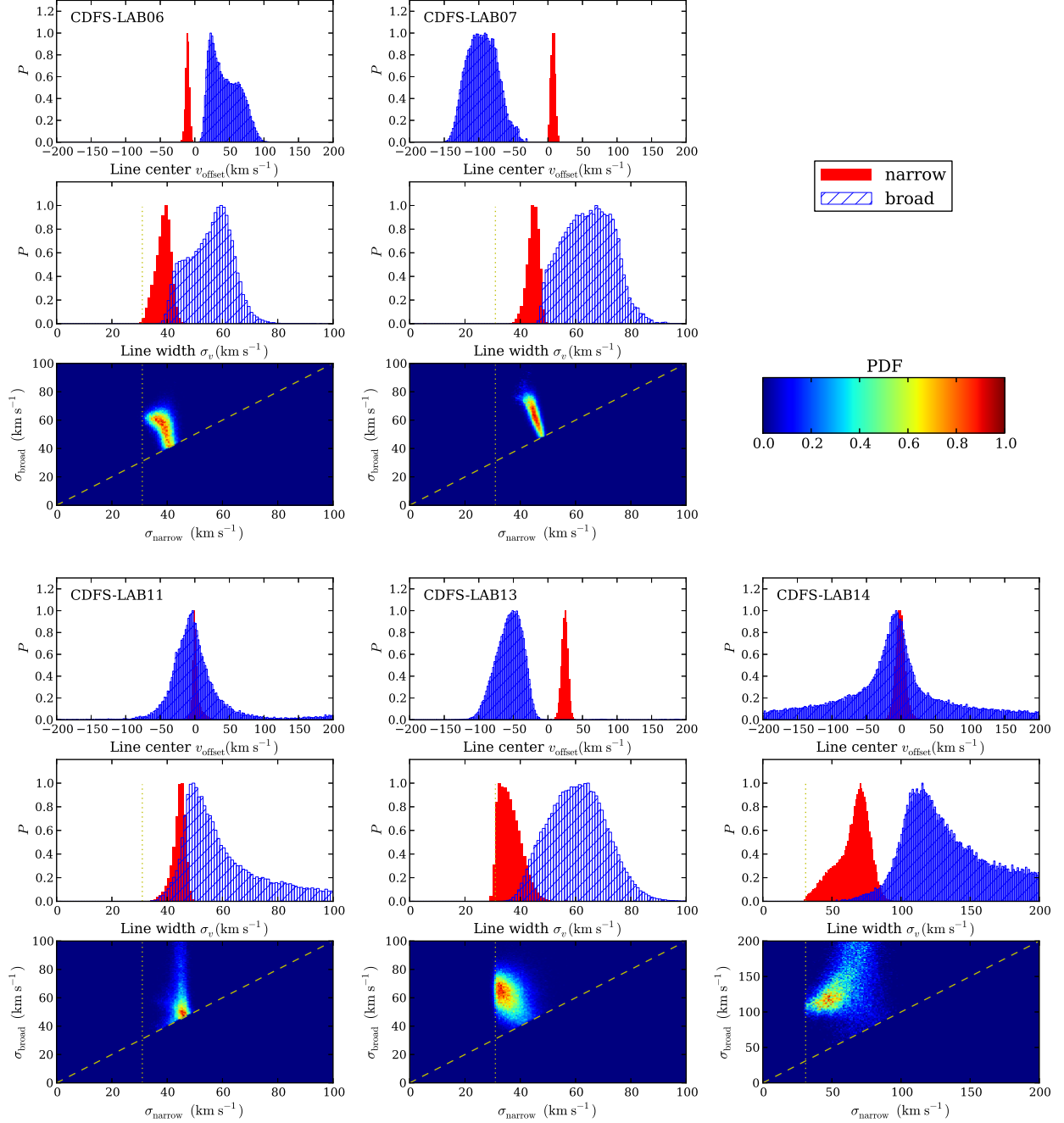


Figure 11. (*Top and middle*) Marginalized likelihood distributions of the line centers and widths of the two Gaussian components. (*Bottom*) Joint 2-D likelihood distributions of the line widths of the two Gaussian components. The red and blue histograms represent the narrow and broad component, respectively. The vertical dotted lines indicate the instrumental resolution ($\sigma_{\text{instr}} = 31 \text{ km s}^{-1}$). The dash lines represent the locus for $\sigma_{\text{narrow}} = \sigma_{\text{broad}}$.

than that of the broad component. The latter two priors are imposed to prevent the MCMC chains from getting stuck in parameter spaces with extremely broad lines but with negligible fluxes.

In Figure 11, we show the likelihood distributions of the line widths of the two components: σ_{narrow} and σ_{broad} . Note that we exclude CDFS-LAB10 in this analysis because its neighboring galaxy (CDFS-LAB10A) makes it difficult to reliably extract its profile (see Sections 3.5.3 and 3.7). Except for CDFS-LAB11, the likelihood distributions of the two line-widths do not overlap significantly, and the peaks of the joint 2-D distributions are not located near the $\sigma_{\text{narrow}} = \sigma_{\text{broad}}$ line (the dashed line). Therefore, we conclude that the remaining four systems (CDFS-LAB06, 07, 13, 14) are likely to consist of two components. The uncertainties of the parameters are determined from the 68.2% confidence interval of the marginalized distribution.

Table 1
Log of X-shooter Observations and Properties of Sample

Name	$L(\text{Ly}\alpha)^a$ ($10^{43} \text{ erg s}^{-1}$)	$\text{EW}(\text{Ly}\alpha)^a$ (\AA)	Coordinate		Date	Airmass	Seeing (arcsec)	T_{exp} (UVB) (hour)	T_{exp} (NIR) (hour)
			R.A.	decl.					
CDFS-LAB06	1.57 ± 0.07	56 ± 3	03:32:19.78	-27:47:31.5	2011-01-07	1.07	0.80	0.76	0.80
CDFS-LAB07	1.14 ± 0.05	58 ± 3	03:32:03.36	-27:45:24.4	2011-01-06	1.05	0.77	0.76	0.80
					2011-01-06	1.18	0.98	0.76	0.80
					2011-01-28	1.12	0.81	0.76	0.80
CDFS-LAB10	0.71 ± 0.04	318 ± 36	03:32:37.45	-28:02:05.7	2010-11-06	1.00	0.71	0.76	0.80
					2010-11-07	1.00	0.68	0.76	0.80
					2010-11-07	1.08	1.13	0.76	0.80
					2010-11-08	1.08	1.23	0.76	0.80
CDFS-LAB11	1.02 ± 0.04	120 ± 10	03:32:43.25	-27:42:58.3	2011-01-08	1.07	0.75	0.76	0.80
					2011-01-08	1.23	0.85	0.76	0.80
CDFS-LAB13	0.94 ± 0.04	184 ± 25	03:32:32.75	-27:39:06.4	2011-01-07	1.22	0.79	0.76	0.80
					2011-01-08	1.01	0.70	0.76	0.80
CDFS-LAB14	0.93 ± 0.05	67 ± 5	03:32:32.29	-27:41:26.4	2011-01-09	1.07	0.80	0.76	0.80
					2011-01-09	1.24	0.73	0.76	0.80
CDFS-LAB01	8.02 ± 0.24	512 ± 50							
CDFS-LAB02	2.88 ± 0.12	43 ± 2							

Note. — Observations for CDFS-LAB01 and CDFS-LAB02 were presented in Yang et al. (2011).

^a $\text{Ly}\alpha$ Luminosity and EW within an isophot of $5.5 \times 10^{-18} \text{ erg s}^{-1} \text{ cm}^{-2} \text{ arcsec}^{-2}$.

Table 2
Properties of $\text{Ly}\alpha$ Line

Name	Red Peak			Blue Peak			Profile ^b
	$\Delta v_{\text{Ly}\alpha}$ (km s^{-1})	σ_v^a (km s^{-1})	Flux ($10^{-17} \text{ erg s}^{-1} \text{ cm}^{-2}$)	v_{offset} (km s^{-1})	σ_v^a (km s^{-1})	Flux ($10^{-17} \text{ erg s}^{-1} \text{ cm}^{-2}$)	
CDFS-LAB01	-65 ± 20	228 ± 14	45.2 ± 1.6	(1) ^c
CDFS-LAB11	84 ± 6	79 ± 3	26.5 ± 0.7	(1) ^c
CDFS-LAB10	247 ± 147	425 ± 97	18.7 ± 2.4	(1) ^d
CDFS-LAB13	152 ± 14	100 ± 9	13.7 ± 0.7	-277 ± 8	43 ± 8	4.0 ± 0.5	(2)
CDFS-LAB06	123 ± 15	150 ± 13	25.7 ± 1.3	(1)
CDFS-LAB02	211 ± 43	192 ± 35	8.2 ± 0.9	-342 ± 117	273 ± 137	3.3 ± 1.3	(2)
CDFS-LAB07	181 ± 15	168 ± 10	22.2 ± 0.8	(1)
CDFS-LAB14	371 ± 34	202 ± 24	18.0 ± 1.2	-404 ± 17	176 ± 18	12.4 ± 1.1	(3)

^a Corrected for the instrumental profile in the UVB ($\sigma_{\text{instr}} \simeq 39 \text{ km s}^{-1}$).

^b Line morphology: (1) single (red) peak, (2) double peaked profile with a stronger red peak, (3) double peaked profile with similar intensity peaks.

^c The profiles of CDFS-LAB01 and 11 are not significantly broader than the $[\text{O III}]$ lines.

^d The profile of CDFS-LAB10 is composed of multiple components (Figure 4). Here the total integrated profile is used for the fit.

Table 3
Decomposition of $[\text{O III}]$ Profile

Name	σ_{narrow}^a (km s^{-1})	v_{broad} (km s^{-1})	σ_{broad} (km s^{-1})	$F_{\text{broad}}/F_{\text{narrow}}^b$	$F_{\text{broad}}/F_{\text{total}}^c$	Δv_{max}^d (km s^{-1})
CDFS-LAB06	38 ± 3	$+39 \pm 27$	55 ± 10	$0.51^{+0.58}_{-0.29}$	0.35 ± 0.17	152 ± 15
CDFS-LAB07	44 ± 2	-97 ± 23	64 ± 10	$0.44^{+0.31}_{-0.18}$	0.32 ± 0.12	222 ± 11
CDFS-LAB13	35 ± 5	-56 ± 21	60 ± 11	$0.84^{+0.55}_{-0.38}$	0.46 ± 0.13	174 ± 18
CDFS-LAB14	67 ± 16	-12 ± 71	125 ± 40	$0.47^{+0.66}_{-0.20}$	0.33 ± 0.20	262 ± 75
CDFS-LAB10	71 ± 1
CDFS-LAB11	47 ± 1

^a The line widths (σ_{narrow} and σ_{broad}) are *not* corrected for the instrumental profile, because some of the line widths are comparable to the instrumental resolution ($\sigma_{\text{instr}} \simeq 31 \text{ km s}^{-1}$ in the NIR).

^b F_{broad} and F_{narrow} are the fluxes in the broad and narrow components of the $[\text{O III}]$ emission line, respectively.

^c $F_{\text{total}} = F_{\text{narrow}} + F_{\text{broad}}$.

^d The maximum blueshifted velocity $\Delta v_{\text{max}} \equiv |v_{\text{broad}} - 2\sigma_{\text{broad}}|$. For CDFS-LAB06 where the broad component is redshifted, we list $|v_{\text{broad}} + 2\sigma_{\text{broad}}|$.